

RESEARCH ARTICLE

Combinatorial patterns of graded RhoA activation and uniform F-actin depletion promote tissue curvature

Marlis Denk-Lobnig¹, Jan F. Totz^{2,3}, Natalie C. Heer¹, Jörn Dunkel² and Adam C. Martin^{1,*}

ABSTRACT

During development, gene expression regulates cell mechanics and shape to sculpt tissues. Epithelial folding proceeds through distinct cell shape changes that occur simultaneously in different regions of a tissue. Here, using quantitative imaging in *Drosophila melanogaster*, we investigate how patterned cell shape changes promote tissue bending during early embryogenesis. We find that the transcription factors Twist and Snail combinatorially regulate a multicellular pattern of lateral F-actin density that differs from the previously described Myosin-2 gradient. This F-actin pattern correlates with whether cells apically constrict, stretch or maintain their shape. We show that the Myosin-2 gradient and F-actin depletion do not depend on force transmission, suggesting that transcriptional activity is required to create these patterns. The Myosin-2 gradient width results from a gradient in RhoA activation that is refined through the balance between RhoGEF2 and the RhoGAP C-GAP. Our experimental results and simulations of a 3D elastic shell model show that tuning gradient width regulates tissue curvature.

KEY WORDS: Actomyosin, Morphogenesis, RhoGAP, RhoGEF, Tissue folding, Transcriptional patterning, *Drosophila*

INTRODUCTION

During development, the three-dimensional shape of a complex organism is generated, in part, by gene expression patterns that are encoded by a one-dimensional sequence of nucleotides in the genome. Patterns of gene expression and resulting signaling processes overlap and interact in space and time to define the function of each cell. For example, morphogen gradients encode positional information for specific cell fates (Dubuis et al., 2013; Rogers and Schier, 2011; Wolpert, 1969). For tissues to obtain their final and functional state, cell fates, shapes and mechanics all need to be positionally specified. Cell fate and mechanical patterns need not be identical, as mechanical properties are often patterned within cells of the same type (Mongera et al., 2018; Sui et al., 2018; Sumigray et al., 2018). Each tissue shape change requires coordinated changes in cell shape and/or position across the tissue, which have to be tailored to the morphological and functional requirements of the tissue while being robust and reproducible

between individual organisms (Chanet et al., 2017; Hong et al., 2016; von Dassow and Davidson, 2009).

Mesoderm invagination in the early *Drosophila melanogaster* embryo involves folding an epithelial sheet and is an established model system for gene expression patterning and morphogenesis (Leptin, 2005). Apical constriction is a cell shape change driven by actomyosin contractility that converts columnar epithelial cells to a wedge shape, which promotes mesoderm invagination (Leptin and Grunewald, 1990; Sweeton et al., 1991). Apical constriction is coordinated across the presumptive mesoderm; there is a spatial, ventral-dorsal gradient of apical non-muscle Myosin-2 (myosin) and apical constriction that extends ~5-6 cell rows on either side of the ventral midline (Heer et al., 2017; Lim et al., 2017; Oda and Tsukita, 2001; Spahn and Reuter, 2013) (Fig. 1A). Beyond this gradient, apical myosin reaches a baseline low level, and 2-4 cell rows (rows ~7-9) stretch their apical surface and bend towards the forming furrow (Heer et al., 2017; Leptin and Grunewald, 1990; Sweeton et al., 1991). In contrast, more dorsal cells, which are part of the neighboring ectoderm, maintain an almost constant apical area throughout the folding process instead of stretching, despite low, baseline-level myosin (Rauzi et al., 2015). We investigated how this tissue-wide pattern of cell shapes is established, by examining the distribution of cytoskeletal proteins across the mesoderm.

Mesoderm cell shape change and cell fate are initially driven by the transcription factors Dorsal, Twist and Snail (Boulay et al., 1987; Furlong et al., 2001; Leptin, 1991; Thisse et al., 1988), which exhibit distinct expression patterns. Nuclear Dorsal is present in a ventral-dorsal gradient that narrows over time (Rahimi et al., 2019; Roth et al., 1989; Rushlow et al., 1989; Steward, 1989; Steward et al., 1988). Twist is a transcriptional activator and some of its targets have a graded expression pattern along the ventral-dorsal axis (Heer et al., 2017; Lim et al., 2017; Rahimi et al., 2019). Snail can both activate and repress gene expression (Rembold et al., 2014). One gene that is activated by Snail is the G-protein coupled receptor (GPCR) Mist (Mthl1; Manning et al., 2013). In contrast to graded Twist target expression, Mist mRNA expression is uniform across the mesoderm (Lim et al., 2017). Therefore, Twist and Snail target genes appear to have distinct patterns of expression.

The product of the Twist target gene *fog* activates the Mist GPCR and a uniformly expressed GPCR, Smog (Costa et al., 1994; Kerridge et al., 2016; Manning et al., 2013). This GPCR pathway and T48 expression act via the guanine nucleotide exchange factor (GEF) RhoGEF2 and the small GTPase RhoA (Rho1) to activate myosin contractility (Barrett et al., 1997; Hacker and Perrimon, 1998; Kolsch et al., 2007). Functioning in opposition to RhoGEF2 to shut off RhoA signaling activity is the RhoA GTPase-activating protein (GAP) C-GAP (also called Cumberland-GAP or RhoGAP71E) (Mason et al., 2016). RhoA coordinately activates both myosin, via Rho-associated and coiled coil kinase (ROCK), and actin filament (F-actin) assembly, via the formin Diaphanous, which function together to mediate cell contractility (Murrell et al.,

¹Biology Department, Massachusetts Institute of Technology, 77 Massachusetts Ave., Cambridge, MA 02139, USA. ²Mathematics Department, Massachusetts Institute of Technology, 77 Massachusetts Ave., Cambridge, MA 02139, USA.

³Department of Mechanical Engineering, Massachusetts Institute of Technology, 77 Massachusetts Avenue, Cambridge, MA 02139, USA.

*Author for correspondence (acmartin@mit.edu)

ORCID: M.D.-L., 0000-0001-6546-3442; J.F.T., 0000-0003-4961-1630; N.C.H., 0000-0002-6003-9981; J.D., 0000-0001-8865-2369; A.C.M., 0000-0001-8060-2607

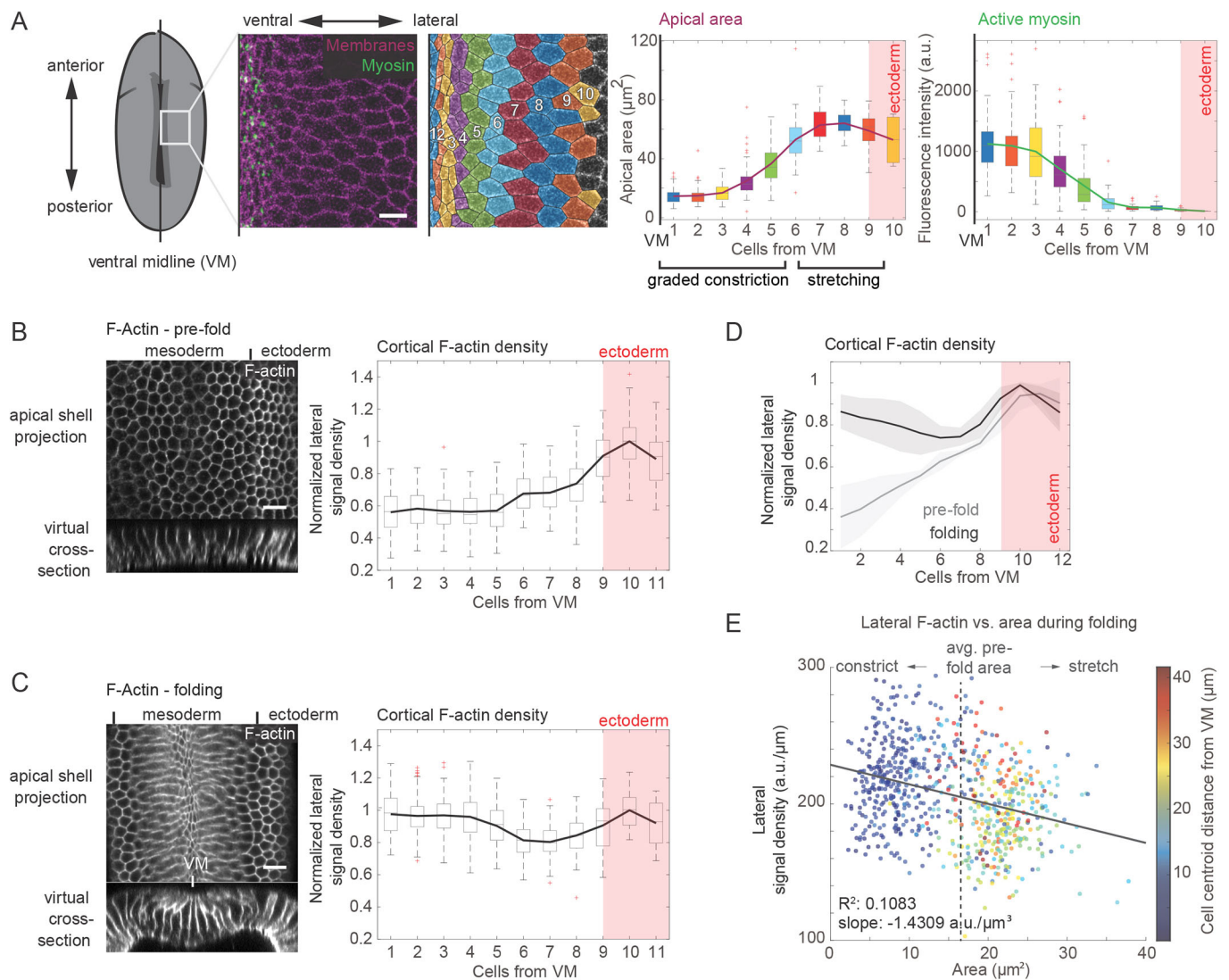


Fig. 1. Lateral F-actin exhibits a distinct distribution from apical myosin. (A) Apical myosin pattern. Images are apical surface view of embryo labeled with sqh::GFP (Myosin) and Gap43::mCherry (Membranes) and segmented example of embryo with cell rows highlighted in different colors, which corresponds to colors in plots. Plots show apical area and apical myosin as a function of cell distance from ventral midline. (B) Lateral F-actin is depleted in the mesoderm before apical constriction. Images are *en face* projections (top) and cross-sections (bottom) of Phalloidin-stained embryos. Plot shows lateral F-actin density (signal intensity around lateral cell contacts near the apical surface, normalized to perimeter) for cells binned by position from ventral midline. Data is represented by box-and-whisker plot from representative embryo. $n \geq 40$ cells per bin (median 51.5 cells). (C) Lateral F-actin accumulates in a ventral-dorsal gradient during furrow formation. Images and plots are analogous to (B). $n \geq 15$ cells per bin (median 73 cells). (D) Average lateral F-actin density trace for three embryos corresponding to B (pre-furrow) and C (furrow), normalized to the cell row with the highest mean. Shaded area corresponds to 1 s.d. in each direction. (E) Apical area is anti-correlated with lateral F-actin levels. Quantification of lateral F-actin density per cell (lateral levels normalized by perimeter) for the embryo shown in C was plotted as a function of apical area. Color of data points represents physical distance from ventral midline in μm (red, ectoderm; yellow/green, marginal mesoderm; blue, ventral mesoderm). Average pre-fold cell area for fixed embryos ($\sim 16 \mu\text{m}^2$ due to shrinkage during fixation) is indicated with dotted gray line. $F=89.172$, $P=4.7014 \times 10^{-20}$ (F-statistic versus constant model), $n=736$ cells. VM, ventral midline. Scale bars: $10 \mu\text{m}$.

2015). Myosin activation occurs in a gradient that is narrower than the gradient of T48 protein accumulation (Heer et al., 2017), but it is not known whether RhoA activation follows a similar pattern to T48 or whether RhoA signaling is refined by its regulators. F-actin is enriched in ventral cells in a manner that depends on RhoA signaling (Fox and Peifer, 2007). We asked whether F-actin displays a multicellular pattern across the mesoderm and how this is controlled transcriptionally and via RhoA signaling.

Here, we characterize a tissue-level pattern of lateral F-actin density that is distinct from apical myosin activation and Twist activity. This pattern of lateral F-actin results from the combination of Snail-dependent depletion and Twist-dependent accumulation, which is tuned by RhoA activity level. We used experimental

perturbations and simulations of a 3D elastic shell model of mesoderm invagination to show that the actomyosin width regulates tissue curvature during folding. Our results show how combinatorial patterning of two transcriptional programs creates distinct zones of cytoskeletal protein accumulation across the mesoderm and that this patterning promotes proper tissue curvature.

RESULTS

Lateral F-actin exhibits a tissue pattern distinct from apical myosin during mesoderm invagination

To determine how the ventral-dorsal pattern of F-actin changes during mesoderm invagination, we labeled F-actin in fixed or live embryos with Phalloidin or Utrophin, respectively, and measured

F-actin in cell bins at defined positions from the ventral midline. We focused our analysis on lateral F-actin density (i.e. total intensity/perimeter in a slice below the medioapical surface), because we observed clear variation of lateral F-actin, but not of medioapical actomyosin density, across the mesoderm-ectoderm boundary (Fig. 1B-D; Figs S1A and S2A,B).

Before onset of ventral furrow formation, mesodermal lateral F-actin density (and integrated intensity) dropped relative to ectoderm cells (Fig. 1B,D; Fig. S1A-C). During ventral furrow formation, lateral F-actin density rose around the ventral midline and exhibited a gradient that extended to cell row 6, similar to apical myosin (Fig. 1C,D; Fig. S1A,C). Increased lateral F-actin density coincided with lateral myosin in the ventral mesoderm, which has been shown to increase lateral tension during invagination (Fig. S2A) (Gracia et al., 2019). At the ventral midline, medioapical F-actin and myosin showed a fibrous organization, as has been previously shown (Fig. S2A) (Coravos and Martin, 2016; Mason et al., 2013). Lateral F-actin density remained lower ~6-8 cell rows from the midline, forming a zone of lateral F-actin depletion relative to the neighboring ectoderm (Fig. 1C; Fig. S1A, C). This contrasts with medioapical myosin and F-actin, and lateral myosin, which showed similar intensity and structure across the mesoderm-ectoderm boundary (Fig. 1A; Fig. S2A,B) (Heer et al., 2017; Lim et al., 2017; Spahn and Reuter, 2013). The observed pattern was also present in live embryos expressing the actin-binding domain of Utrophin fused to green fluorescent protein (Utrophin::GFP) or mCherry (Utrophin::mCherry), but not with a general membrane marker, Gap43::mCherry, or cortical Diaphanous, indicating that this measurement is not a fixation artifact or due to changes in plasma membrane structure, such as stretching (Fig. S1D; Fig. S2C). Thus, lateral F-actin exhibits a distinct pattern from apical myosin activation.

The observed tissue-wide pattern of lateral F-actin density matched the pattern of apical cell area constriction and stretching (Fig. 1A,C; Fig. S1A). To quantify the strength of this relationship, we correlated lateral cell F-actin density with apical cell area across mesoderm and adjacent ectoderm cells (Fig. 1E). We found that lateral F-actin density and apical area were anti-correlated, in part, because marginal mesoderm cells had low F-actin and were stretched and adjacent ectoderm cells had intermediate F-actin density and did not stretch or constrict. Because F-actin density and turnover influence the ability to dissipate stress (Clement et al., 2017; Salbreux et al., 2012; Stricker et al., 2010), our result suggests that lower F-actin density allows marginal mesoderm cells to stretch, leading to an inverted cell morphology for cells at the edge of the mesoderm compared with apically constricted cells at the ventral midline.

Snail and Twist regulate distinct components of the F-actin pattern

To determine how this tissue-wide F-actin pattern is established, we tested how the transcription factors Snail and Twist affect lateral F-actin density. Snail activity in the mesoderm, as measured by *mist* transcription, is uniform (Lim et al., 2017) and we found that the Snail boundary co-localized precisely with the F-actin depletion boundary (Fig. 2A). We then quantified lateral F-actin density in *snail* and *twist* mutants (Fig. S3A). Unlike control (heterozygous) embryos, *snail* homozygous mutant embryos expressing fluorescently tagged Utrophin did not exhibit patterned lateral F-actin density in the ventral region, but rather changes in intensity that smoothly dropped off towards the edge of the imaged region in all embryos (Fig. 2B,C). Because *snail* mutant embryos were imaged live, we could identify the mesoderm/ectoderm boundary based on subsequent germband

extension movements in the ectoderm and premature cell divisions that occurred in the uninternalized mesoderm, which is mitotic domain 10 (Foe, 1989; Grosshans and Wieschaus, 2000). In addition, we fixed and Phalloidin-stained *snail* mutants and made manual cross-sections, which failed to show a domain of F-actin depletion, unlike equivalently staged control embryos (Fig. S3B). Thus, Snail is required to decrease lateral F-actin density in the mesoderm.

In contrast to Snail, the expression of Twist transcriptional targets is graded, with Twist target expression initiating first along the ventral midline and then expanding more dorsally (Lim et al., 2017; Rahimi et al., 2019). Twist also regulates *snail* expression; *twist* mutants reduce *snail* expression width (Leptin, 1991). To determine the requirement of *twist* for the tissue-wide pattern of lateral F-actin, we examined lateral F-actin density in a *twist* null mutant. We used the transient myosin contractions that occur in *twist* mutant mesoderm cells to identify the position of the mesoderm (Martin et al., 2009). In contrast to *snail* mutants, *twist* mutant embryos exhibited lower lateral F-actin density in the mesoderm and a clear boundary with the ectoderm (Fig. 2D,E,F). However, the zone of low lateral F-actin was decreased to half the normal width, consistent with narrowed *snail* expression depleting F-actin in a narrower mesoderm. Graded F-actin accumulation around the ventral midline was absent in *twist* mutants, suggesting that higher lateral F-actin density at the midline depends on the Twist pathway, which includes RhoA activation (Dawes-Hoang et al., 2005; Fox and Peifer, 2007; Kolsch et al., 2007; Mason et al., 2013). Therefore, mesodermal control of lateral F-actin by Twist and Snail is comprised of two nested layers: (1) before ventral furrow formation, uniform Snail activity lowers lateral F-actin density across the mesoderm, and (2) during ventral furrow formation there is a Twist-dependent increase in lateral F-actin density that, similar to apical myosin, creates a ventral-dorsal gradient, but also creates a ‘valley’ in lateral F-actin density at the margin of the mesoderm.

Neither graded myosin activation nor F-actin depletion depend on adherens junctions

Our data suggested that Snail and Twist promote uniform mesodermal F-actin depletion before apical constriction and subsequent graded actomyosin accumulation, respectively. In the ventral furrow and the related process of *Drosophila* posterior midgut formation, it has been shown that mechanical feedback between cells can regulate myosin accumulation (Bailles et al., 2019; Fernandez-Gonzalez et al., 2009; Mitrossilis et al., 2017), which could contribute to this gradient or wave in contractility. Furthermore, adherens junctions (AJs) are a known target of Snail in the mesoderm (Chanet and Schweisguth, 2012; Dawes-Hoang et al., 2005; Kolsch et al., 2007) and E-cadherin exhibits a similar tissue-level pattern to F-actin (Fig. S4A). Therefore, it was important to determine whether the actomyosin patterns depended on AJs, force transmission or more autonomous transcriptional activity inside cells.

To determine the contribution of AJs to the multicellular patterns of myosin activation and lateral F-actin density, we depleted α -catenin by RNA interference (α -catenin RNAi), which disrupted AJs and uncoupled mechanical connections between cells (Fig. 3A; Movies 1 and 2), similar to past studies (Fernandez-Gonzalez and Zallen, 2011; Levayer and Lecuit, 2013; Martin et al., 2010; Yevick et al., 2019). In α -catenin RNAi embryos, ventral cell apical areas remained at pre-gastrulation levels ($\sim 40 \mu\text{m}^2$) and AJ protein localization was severely disrupted, demonstrating the efficacy of the knockdown (Fig. 3A,B; Fig. S4B,C). Medioapical myosin reproducibly accumulated in a gradient around the ventral midline that was similar to the wild-type gradient (Fig. 3C,E; Fig. S4E).

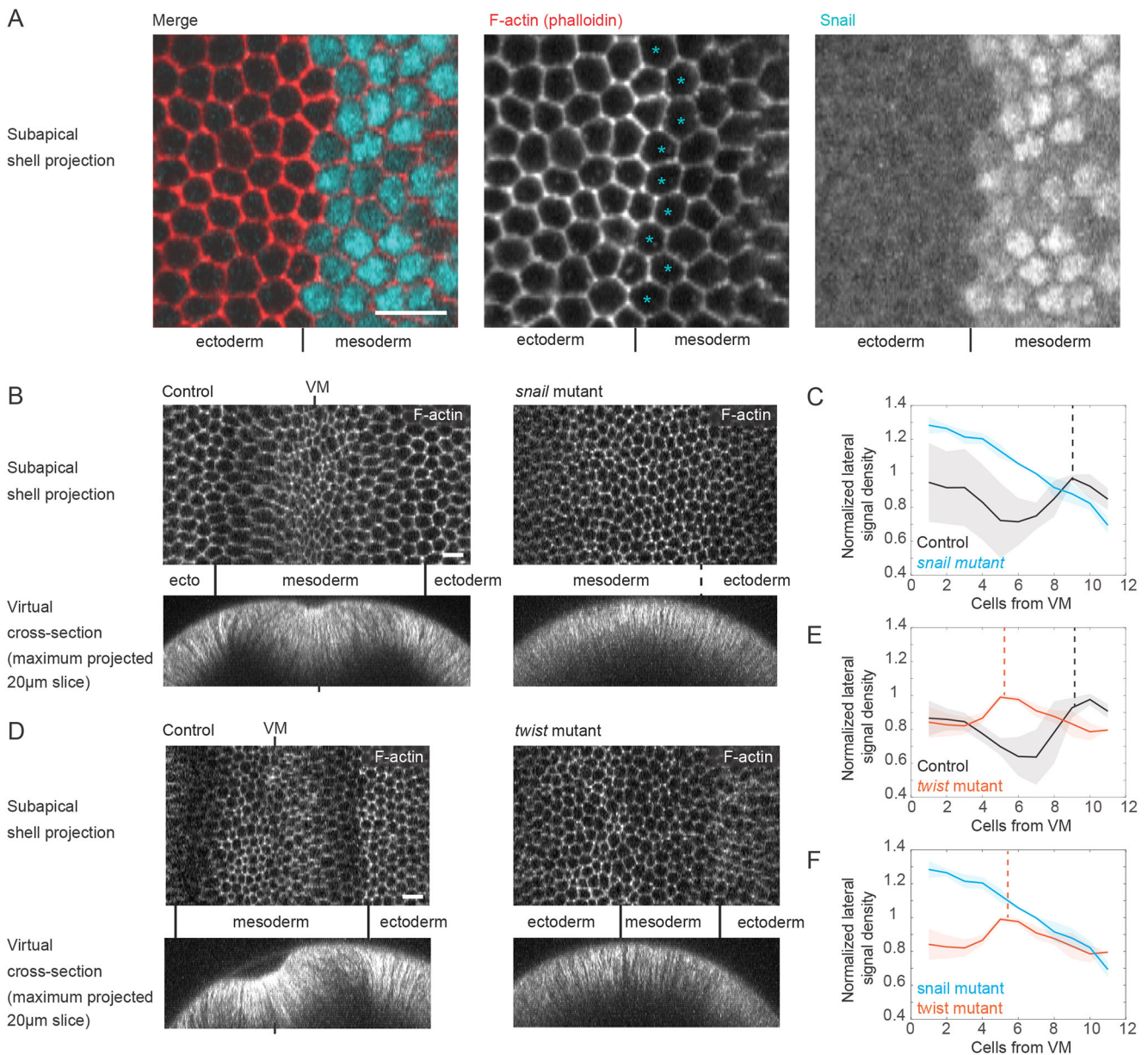


Fig. 2. *Snail* and *Twist* regulate distinct features of the tissue-wide F-actin pattern. (A) *Snail* expression boundary corresponds to F-actin depletion boundary. Images are from anti-*Snail*- and Phalloidin-stained embryo. Cyan asterisks in F-actin image designate *Snail*-positive cells bordering the ectoderm. (B) The *snail* mutant disrupts mesodermal F-actin depletion. Top images are subapical (~15 μ m below apical surface) shell-projections from representative live homozygous *snail* mutant and normal sibling embryo expressing *Utrophin::mCherry* (F-actin). In addition, to illustrate the F-actin pattern independent of choosing a single cross-sectional slice, we show a virtual cross section which is a projection of multiple slices along the anterior-posterior axis (bottom). (C) Quantification of lateral F-actin density by cell row from three *snail* mutant and three normal sibling embryos (mean \pm s.d.). All *snail* mutants lack F-actin patterning. All traces were normalized to the highest-mean ectodermal cell bin before averaging. Dashed line designates approximate mesoderm-ectoderm boundary in control embryos. (D) The *twist* mutant exhibits F-actin depletion, but lacks F-actin elevation around midline. Images are subapical shell-projections from three representative live homozygous *twist* mutant and three normal sibling embryos expressing *Utrophin::mCherry* (F-actin). (E) Quantification of lateral F-actin density from three *twist* mutant and three normal sibling embryos (mean \pm s.d.). All traces were normalized to their highest-mean ectodermal cell bin before averaging. Dashed lines mark respective transitions from low F-actin to high F-actin regions of the tissue. (F) Mean F-actin lateral density \pm s.d. for three *twist* and three *snail* mutant embryos. Dashed line indicates transition from low to high F-actin regions. VM, ventral midline. Scale bars: 10 μ m (A,B,D).

Therefore, graded myosin activation across the tissue does not require sustained mechanical connectivity between cells.

Next, we determined whether mesodermal F-actin depletion depended on intact AJs. Similar to wild-type embryos, lateral F-actin density in α -catenin RNAi embryos was depleted across the mesoderm with a sharp boundary to the ectoderm (Fig. 3D,E, Fig. S4E). This observation suggests that *Snail*-mediated F-actin density reduction does not depend on intact AJs. Furthermore, low

lateral F-actin density in marginal mesoderm cells was maintained despite a lack of apical constriction and stretching of marginal mesoderm cells, confirming that reduced F-actin density in these cells was not due to cell stretching. In contrast, lateral F-actin density around the midline did not increase in α -catenin RNAi embryos as in wild-type embryos during constriction. The lack of elevated lateral F-actin density in α -catenin RNAi embryos may be because of disrupted AJs, which were concentrated in apical

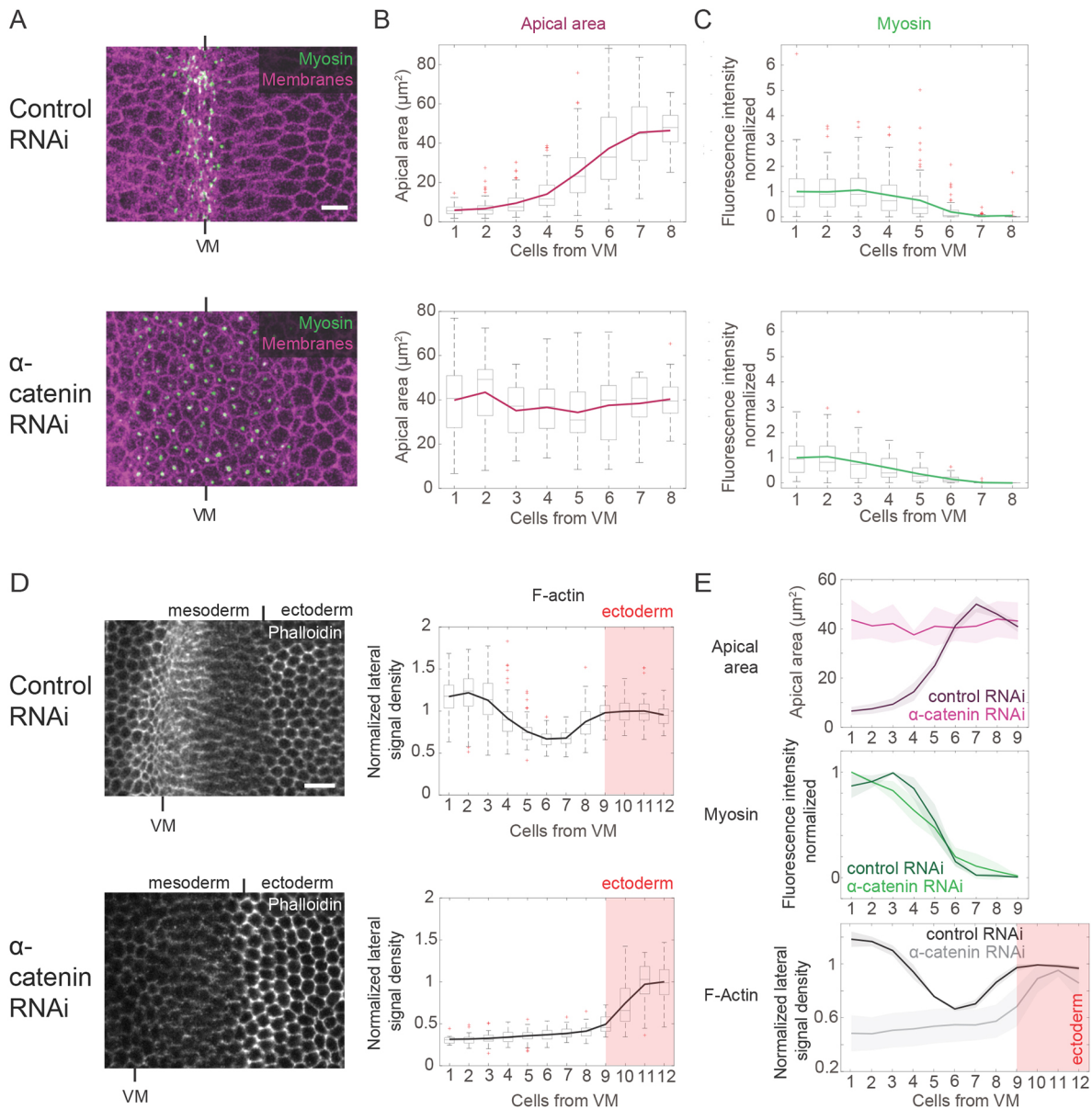


Fig. 3. Myosin gradient and uniform F-actin depletion do not require adherens junctions. (A) *En face* projections of control (Rh3 RNAi) and α -catenin RNAi embryos expressing sqh::GFP (Myosin, green) and Gap43::mCherry (Membranes, magenta). (B,C) Quantification of apical area (magenta, B) and normalized apical active myosin (green, C) as box-and-whisker plots (colored line indicates mean) where each bin is a cell row at a given distance from the ventral midline (VM) [$n \geq 41$ (control) or 44 (α -catenin RNAi) cells per row; median 72 (control) or 107 (α -catenin RNAi) cells]. (D) Left: Images of Phalloidin-stained control (Rh3 RNAi, top) and α -catenin RNAi (bottom) embryos focused on the mesoderm-ectoderm boundary. Right: Same as B, but cell bins are ectoderm-normalized lateral F-actin density [$n \geq 52$ (control) or 8 (α -catenin RNAi) cells per row; median 78 (control) or 40.5 (α -catenin RNAi) cells]. (E) Mean \pm s.d. traces for control and α -catenin RNAi embryos. Top: Average apical area behavior ($n=4$ embryos per condition). Middle: Average apical myosin intensity behavior ($n=4$ embryos per condition). Bottom: Average lateral F-actin density ($n=3$ embryos per condition). Scale bars: 10 μm .

spots that also contained myosin and F-actin in mesoderm cells (Fig. S4B-D), but it is also possible that the increased lateral F-actin density at the midline in wild-type/control embryos requires apical constriction. These results suggest that mesodermal F-actin depletion in the mesoderm does not require intact AJs, which is consistent with transcriptional regulation driving the observed pattern.

Myosin pulses elicit different area responses in midline versus marginal mesoderm cells

To understand how the constriction and stretching pattern across the ventral furrow is generated, we then characterized how the dynamics

of myosin and cell behavior vary across the tissue. Apical myosin in mesoderm cells accumulates as a series of pulses – discrete events in which there is a burst of myosin accumulation and constriction of the cell apex (Martin et al., 2009). There are distinct classes of myosin pulses that occur during furrow formation. ‘Ratcheted pulses’ are events in which apical, active myosin persists after a pulse and decreased apical area is sustained (Fig. 4A) (Xie and Martin, 2015). In contrast, ‘unratcheted pulses’ exhibit myosin dissipation after the pulse and cell relaxation follows constriction. There is a continuum of behaviors from ratcheted to unratcheted, which are associated with low and high C-GAP expression, respectively (Mason et al., 2016).

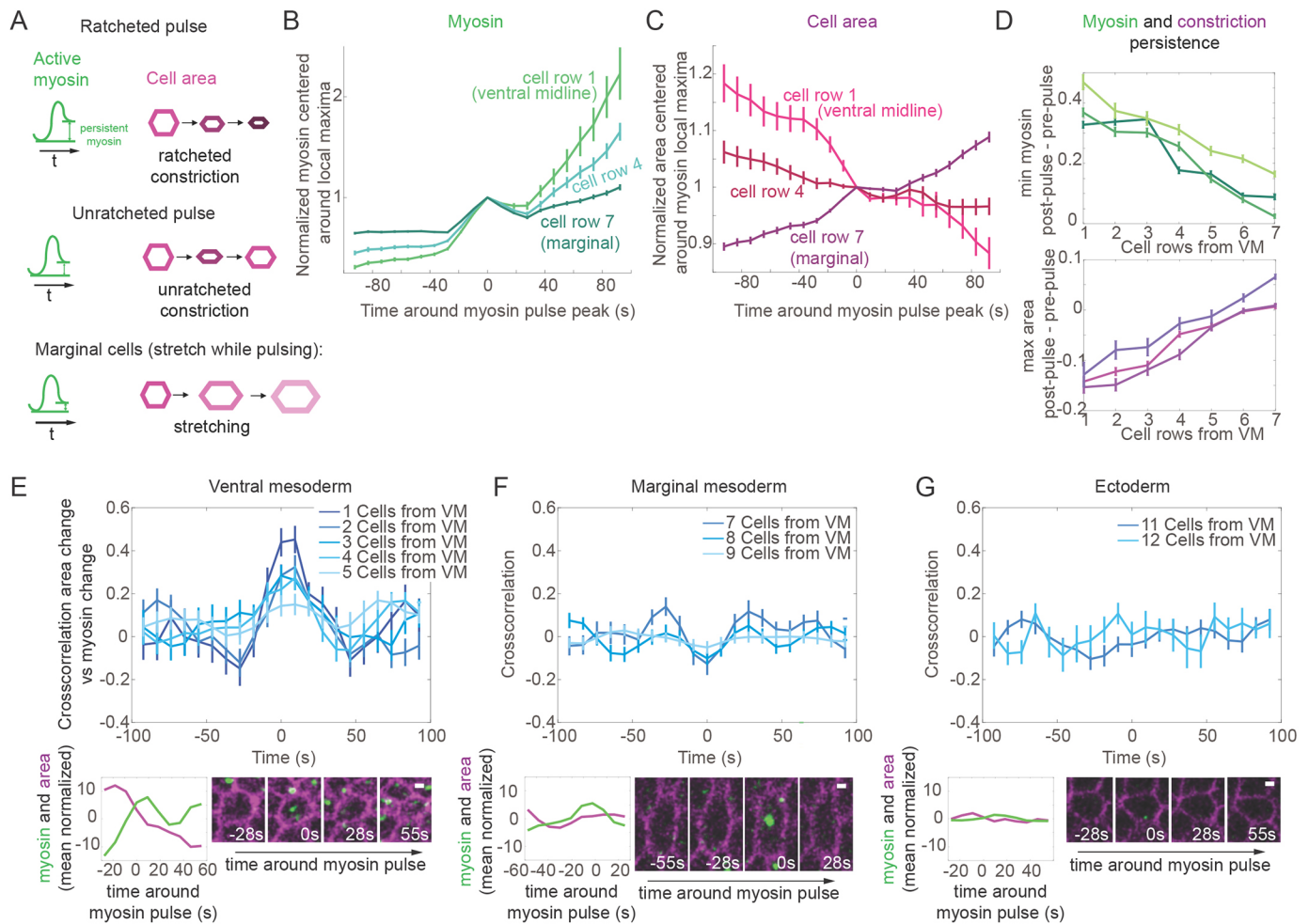


Fig. 4. Contractile dynamics vary with distance from ventral midline. (A) Diagram categorizing types of dynamic cell behaviors observed during ventral furrow formation. ‘Ratcheted’ pulses: Constricted cell shape stabilized and apical myosin levels increase. ‘Unratcheted’ pulses: Constricted cell shape reversed after pulse and apical myosin levels return to baseline. Marginal cells: Cells exhibit little constriction and myosin levels return to baseline after pulse. (B,C) Mean \pm s.e.m. of apical myosin intensity (B) and apical area (C) around pulses (local maxima in myosin accumulation rate) for cell row 1 at the ventral midline (VM), cell row 4 within the myosin gradient and marginal mesoderm cell row 7 shown for one representative embryo. Analysis of 106 pulses for cell row 1; 192 pulses for cell row 4; 335 pulses for cell row 7. (D) Mean \pm s.e.m. for persistence of myosin (minimum myosin 0-100 s after pulse – minimum myosin 0-100 s before pulse) and area (maximum area 0-100 s after pulse – maximum area 0-100 s before pulse) by bin (distance from the midline) for three embryos. $n \geq 83$ pulses per cell row in each embryo (median 192, 238 and 343 pulses per cell row for the three embryos, respectively). (E-G) Top: Cross-correlation of myosin rate and constriction rate averaged by cell bin; split up by ventral mesoderm (cell rows 1-5, E), marginal mesoderm (cell rows 7-9, F) and ectoderm (cell rows 11 and 12, G). At least 21 cells per cell row were analyzed, median 32 cells per cell row. Bottom: Myosin (green) and apical area (magenta) traces (normalized to average) and images of representative individual cells during a myosin pulse, for each region. Scale bars: 2 μ m.

To determine whether myosin pulse types vary across the ventral-dorsal axis, we examined myosin persistence in different cell rows. Consistent with previous measurements of contractile pulses in the middle of the ventral furrow (Xie and Martin, 2015), pulses close to the ventral midline exhibited persistent myosin; the myosin level after the pulse was higher than the initial baseline (Fig. 4B, cell row 1). Myosin persistence was associated with a sustained decrease in apical area (Fig. 4C, cell row 1) (Xie and Martin, 2015). In contrast, myosin pulses at the margin of the mesoderm did not exhibit strong myosin persistence (Fig. 4B, cell row 7). These myosin pulses accompanied cell stretching and did not robustly result in cell apex constriction (Fig. 4C, cell row 7). Comparing pulse behavior across different ventral-dorsal positions, we found a graded decrease in myosin persistence and area stabilization after pulses with distance from the ventral midline (Fig. 4D).

To further differentiate myosin pulse behaviors, we compared the cross-correlation between the constriction rate and the rate of myosin change in cells along the ventral-dorsal axis. Cells closest to the ventral midline exhibited the strongest positive correlation, indicating a correspondence between myosin increase and constriction (Fig. 4E). Peak correlation was highest in cells along the ventral midline and decreased gradually as distance from the ventral midline increased (Fig. 4E). Cells ~7-8 rows from the midline exhibited a small negative correlation, indicating that these cells are not prone to constricting, and may even increase their area during myosin pulses (Fig. 4F). This behavior was specific to mesoderm cells at this stage because ectoderm cells did not exhibit either a clear positive or negative correlation (Fig. 4G, cell rows 11, 12). This suggests that there is a gradient in cell behaviors coincident with myosin pulses, which we hypothesize contributes to the transition from constricting to stretching with distance from the midline.

RhoA activation occurs in a gradient

We next investigated how the patterns in apical myosin and lateral F-actin accumulation are regulated by biochemical signaling. Because Twist functions upstream of RhoA, we examined fluorescently tagged versions of the RhoA activator RhoGEF2 (under an endogenous promoter), the Anillin Rho-binding domain (an active RhoA sensor) and the RhoA effector ROCK (Mason et al., 2016; Munjal et al., 2015; Simoes Sde et al., 2010) (Fig. 5A). Each of these fluorescent protein markers became apically enriched in ventral cells during ventral furrow formation, consistent with previous studies (Fig. 5B) (Kolsch et al., 2007; Mason et al., 2013, 2016). Quantification of apical fluorescence by cell row revealed that all three markers for RhoA pathway activation were graded along the ventral-dorsal axis, exhibiting strong fluorescence at the ventral midline and gradually decreasing to baseline after ~6 cells (Fig. 5B,C; Fig. S5A). In contrast, endogenously tagged C-GAP-GFP appeared uniform across the ventral domain during folding (Fig. S5B). Therefore, there is a ventral-dorsal gradient of RhoA activation in the mesoderm. We next tested how the RhoA activity affects graded apical myosin.

RhoGEF2 and C-GAP modulate actomyosin gradient width

The gradient in accumulated T48 transcripts and protein extends beyond the 5-6 cell rows from the ventral midline where we detect RhoA and myosin activation (Heer et al., 2017; Lim et al., 2017; Rahimi et al., 2019). Mesodermal RhoA signaling is required for apical myosin accumulation and includes an activator/inhibitor pair (Dawes-Hoang et al., 2005; Mason et al., 2016; Nikolaidou and Barrett, 2004). Therefore, we hypothesized that the signaling network downstream of T48 further shapes the contractile gradient (Fig. 5A). To test the importance of this circuit in regulating the multicellular patterning of the actin cytoskeleton, we examined actomyosin after manipulating RhoA activation by either depleting C-GAP by RNAi (C-GAP RNAi) or overexpressing RhoGEF2 (RhoGEF2 O/E), which would both be expected to elevate RhoA activity (Fig. S6E). To avoid disrupting subcellular myosin localization, we identified expression conditions that did not grossly disturb cellular actomyosin organization in the mesoderm or ectoderm (Fig. 6A,B; Fig. S6A,B). RhoGEF2 O/E had the greatest effect on myosin accumulation, showing that this was the most consistent way for us to elevate RhoA activity (Fig. S6F).

C-GAP RNAi and RhoGEF2 O/E significantly expanded the myosin gradient width, with myosin activation occurring 1-2 cell rows (or ~5-10 μm) further from the ventral midline than in control embryos (Fig. 6C,D; Fig. S7A,B,E). This coincided with an expanded domain of uniform high myosin per cell around the ventral midline, so that the graded region was moved outward (Fig. S7A,B). RhoGEF2 O/E and C-GAP RNAi expanded the myosin gradient without expanding mesoderm width (Fig. S6C). C-GAP RNAi also expanded the zone of upstream RhoA activation and downstream apical constriction around the ventral midline (Fig. 6C; Fig. S6D; Fig. S7A). We also attempted to lower RhoA signaling with RhoGEF2 RNAi; however, we were unable to generate a strong RhoGEF2 knockdown without disrupting cellularization (Fig. S7G). The strongest knockdown we could achieve without affecting cellularization did not lower myosin levels and did not narrow the myosin gradient (Fig. S7C-F). Overall, our data show that increasing RhoA activity increases the width of the myosin pattern by moving the gradient away from the ventral midline and creating a domain with uniformly high cellular myosin at its center.

To determine whether RhoA activation is crucial for regulation of the lateral F-actin pattern, we examined lateral F-actin density in

mesoderm cells relative to ectoderm after elevating or depleting RhoA activity. Elevating RhoA activation, by RhoGEF2 O/E, significantly increased lateral F-actin density in marginal mesoderm cells, causing them to be more similar to ectoderm cells (Fig. 6G-I). C-GAP RNAi also increased the mean lateral F-actin density in these cells, but this change was not as dramatic, consistent with the lower level of RhoA hyperactivation (Fig. 6E,F,I). In some cases, RhoGEF2 O/E and C-GAP RNAi completely eliminated the pattern of F-actin depletion and elevation across the mesoderm (Fig. 6G,H). When examining RhoGEF2 RNAi embryos, we found that Utrophin::GFP suppressed cellularization defects of RhoGEF2 RNAi, possibly because the Utrophin actin binding domain can stabilize F-actin (Bun et al., 2018). This allowed us to determine that RhoGEF2 RNAi further depleted mean lateral F-actin in marginal mesoderm cells (Fig. 6F,I). Although not statistically significant, the direction of the change is consistent with our other data suggesting that RhoA activity regulates apical myosin gradient width and also the pattern of lateral F-actin density across the mesoderm.

Myosin gradient width regulates furrow curvature and lumen size

To examine the role of the wild-type contractile pattern in ventral furrow formation, we tested how disrupting this pattern affects tissue shape. In wild-type embryos with graded constriction, the ventral furrow was a sharp, v-shaped fold with high curvature at its center (Fig. 7A). Previous work has shown that globally changing cell fate by altering the *dorsal* gradient to expand the mesoderm resulted in a flattened depression (Heer et al., 2017). Here, we tested whether disrupting actomyosin tissue patterning by C-GAP RNAi or RhoGEF2 O/E, which did not affect mesoderm width (Fig. S6C), affects ventral furrow curvature. C-GAP RNAi embryos, in which the zone of uniform constriction around the ventral midline was wider, had lower midline curvature than wild-type embryos (Fig. 7A,C; Fig. S8A,B). RhoGEF2 O/E embryos also had lower midline curvature, suggesting that increased myosin activity, gradient width and/or elevated lateral F-actin density at the mesoderm margin decreases tissue curvature (Fig. 7B,C; Fig. S8A,B). Importantly, despite higher myosin accumulation, there was less apical constriction in RhoGEF2 O/E embryos (Fig. S6F; Fig. S7B). Indeed, we found that myosin gradient width and tissue curvature were anti-correlated across embryos of different genotypes (Fig. 7E). Most embryos still folded successfully, although some extreme cases did not. Successful folding in C-GAP RNAi and RhoGEF2 O/E embryos was associated with a significantly enlarged lumen when the invaginated mesoderm formed a tube (Fig. 7A,B,D).

RhoGEF2 O/E and C-GAP RNAi increased both myosin gradient amplitude and gradient width (Fig. S7A,B,G). To distinguish between the possible effects of these two parameters, we varied patterns of contractility in a three-dimensional continuum mechanical model of ventral furrow formation (Fig. 7F). For this model, we used contractile patterns that were matched to the patterns that we observed for wild-type, RhoGEF2 O/E and C-GAP RNAi, rather than the larger expansion of the mesoderm that we examined previously (Heer et al., 2017). In agreement with our experimental observations, the model predicted that increasing the width of the uniform domain around the ventral midline and moving the gradient outward, independently of myosin amplitude, lowered mean central curvature after the tissue surface reached a 10 μm depth, which corresponded to the depth that we measured curvature *in vivo* (Fig. 7G-I; Fig. S9A-D; Movie 3). Wider gradient width also tended to result in larger, deeper final folds in the simulation (Fig. S9E-H). Conversely, increasing myosin amplitude is

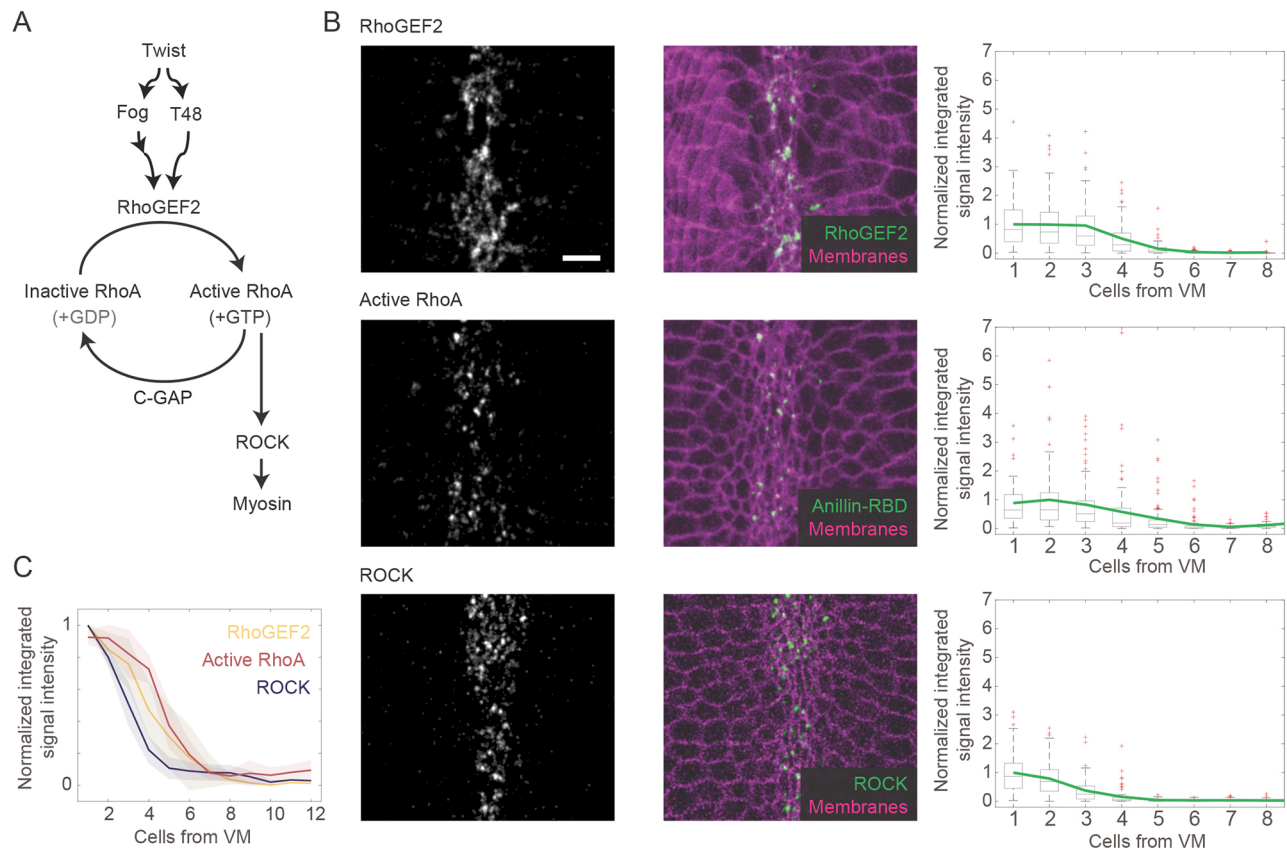


Fig. 5. RhoA activation is graded. (A) Simplified diagram of signaling downstream of Twist. (B) Images of RhoGEF2::GFP (top), Anillin Rho-binding domain::GFP (Active RhoA) (middle) and Rok::GFP (bottom) with Gap43::mCherry (membranes). Ventral midline (VM) in center. Plots (right) are normalized apical RhoGEF2::GFP intensity (top), Anillin Rho-binding domain::GFP intensity (middle), and Rok::GFP intensity (bottom) as a function of distance from the ventral midline for one representative embryo. Data are represented by box-and-whisker plots, where each bin is a cell row at a given distance from the ventral midline. At least 32 cells (RhoGEF2, median 85 cells), 58 cells (Active RhoA, median 76.5 cells) or 51 cells (ROCK, median 68.5 cells) were analyzed for each cell row. Brightness and contrast were adjusted individually to best display the intensity range for each marker. (C) Mean (\pm s.d.) apical fluorescent signal across cell rows for five (RhoGEF2::GFP, Rok::GFP) or four (Anillin Rho-binding domain::GFP) embryos normalized to highest-mean cell row. Scale bar: 10 μ m.

associated with increased mean curvature at the ventral midline at 10 μ m invagination depth (Fig. 7G-I; Fig. S9A-D). Thus, the lower curvature that accompanies RhoA hyperactivation can be mainly explained by increased gradient width.

To further determine the relationship between actomyosin patterning and curvature, we also decreased RhoA activation. RhoGEF2 RNAi in Utrrophin::GFP-expressing embryos enabled us to observe the relationship between lower lateral F-actin density in marginal mesoderm cells and folding (Fig. 6F,I). These embryos had increased mean midline curvature compared with control embryos, which we speculate could be because of the lower F-actin density in the marginal mesoderm cells and/or possibly a narrower F-actin gradient at the midline (Fig. S8A,B). Overall, our data suggest that the multicellular gradient shape and the F-actin density in marginal mesoderm cells influences tissue curvature during ventral furrow formation.

DISCUSSION

Here, we discovered a pattern of lateral F-actin across the *Drosophila* mesoderm and demonstrated how it emerges from the combination of overlapping patterns of transcriptional activity (Fig. 7J). We showed that Snail-dependent uniform depletion of lateral F-actin throughout the mesoderm, plus Twist-dependent lateral F-actin accumulation in a gradient around the ventral midline, pattern F-actin across the ventral side of the embryo. The levels and

dynamics of F-actin and myosin in distinct cell groups are correlated with the cell shape changes. In addition, we found that RhoA regulation by the balance of RhoGEF2 and C-GAP determines the position of the region of graded myosin and the extent of F-actin density depletion as well as the shape of the resulting tissue fold. Although experimentally altering the pattern of contractility also altered overall RhoA activation levels, we explored levels of RhoA activation that did not grossly disrupt myosin polarity and developed a model of ventral furrow formation to demonstrate that myosin pattern width specifically can change tissue curvature. We suggest that differences in F-actin density, turnover and/or myosin persistence between cell groups may determine whether cells undergo apical constriction versus stretching across the ventral domain and thus resulting tissue shape.

Combination of Twist and Snail creates distinct zones of lateral F-actin density

Before folding, we demonstrated that Snail expression results in uniform lateral F-actin depletion in mesoderm cells. During folding, Twist expression results in a gradient of lateral F-actin accumulation in a manner that depends on RhoA signaling and intact AJs. Cells with high lateral F-actin density tend to maintain their shape or constrict, whereas low-F-actin cells stretch. It is possible that this subapical F-actin contributes to stabilizing cell shape after contractile pulses; however, stabilization is also correlated with apical myosin

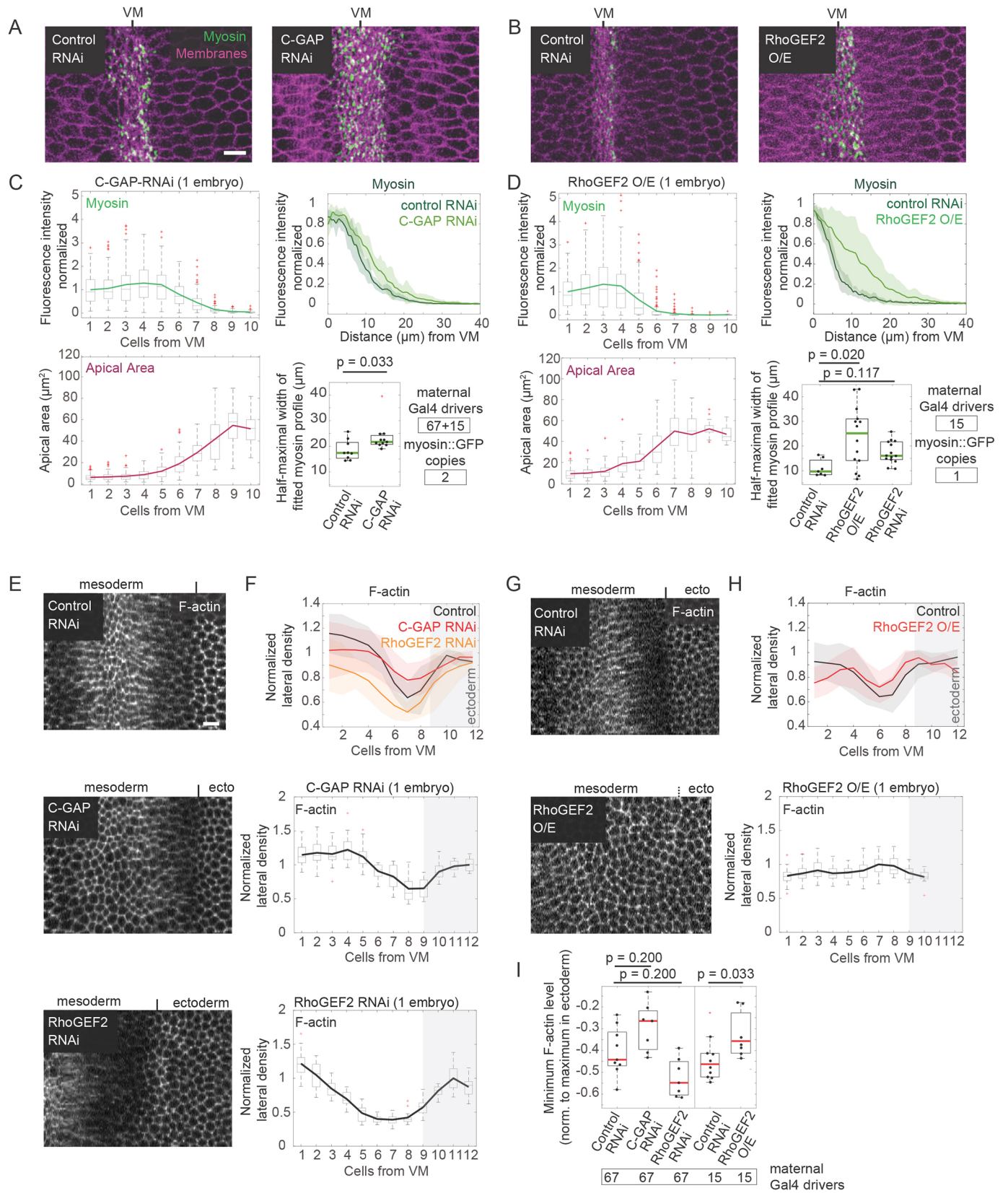


Fig. 6. See next page for legend.

(Xie and Martin, 2015), which is more concentrated in mesoderm cells. The fact that F-actin depletion precludes stretching suggests that F-actin depletion is not a consequence of cell shape.

In the marginal mesoderm, lower F-actin density in stretching cells is compounded by lower levels of zonula adherens proteins (Dawes-Hoang et al., 2005; Kolsch et al., 2007; Weng and

Fig. 6. RhoA hyperactivation widens myosin gradient and elevates F-actin at the mesoderm margin. (A,B) Images (apical shell projections) of control (Rh3 RNAi) and C-GAP RNAi embryos expressing two copies of sqh::GFP (Myosin, green) and one copy of Gap43::mCherry (Membranes, magenta) (A), or control and RhoGEF2 O/E embryos expressing one copy of sqh::GFP (Myosin, green) and Gap43::mCherry (Membranes, magenta) (B). (C,D) C-GAP RNAi and RhoGEF2 O/E embryos have a wider half-maximal gradient position. Left: Box-and-whisker plots (colored line indicates mean) show normalized apical myosin intensity (green) and apical area (magenta) for representative C-GAP RNAi (C, $n \geq 50$ cells/row) and RhoGEF2 O/E embryo (D, $n \geq 23$ cells/row). Right: Mean \pm s.d. of apical myosin intensity as a function of physical distance from midline for control ($n=9$) and C-GAP RNAi ($n=11$) (C) or control ($n=7$) and RhoGEF2 O/E embryos ($n=14$) (D). Box-and-whisker plot (overlaid with data points representing each quantified embryo) below shows calculated half-maximal width of the myosin profile for each condition above as well as RhoGEF2 RNAi (D, $n=14$ embryos). *P*-values were based on Mann–Whitney U test (C) or Kruskal–Wallis+post hoc test (D). (E,G) Images (subapical shell projection) of control (Rh3 RNAi), C-GAP RNAi or RhoGEF2 RNAi embryos (E) or control and RhoGEF2 O/E embryo (G) expressing Utrophin::GFP. (F,H) RhoA activity affects lateral F-actin density in cells at the mesoderm margin. Top: Mean lateral F-actin density \pm s.d. from multiple embryos, normalized to mean of highest ectodermal cell row, for control RNAi ($n=9$), C-GAP RNAi ($n=7$) and RhoGEF2 RNAi ($n=7$) (F) or control RNAi ($n=10$) and RhoGEF2 O/E ($n=7$) (H). Middle: Quantification of normalized lateral F-actin density as a function of distance from ventral midline for a single C-GAP RNAi (F) or RhoGEF2 O/E (H) embryo [$n \geq 9$ cells/row (F,H); median 25.5 cells (F) and 21.5 cells (H)]. Data representation same as in C and D. Bottom: Quantification of normalized lateral F-actin density as a function of distance from ventral midline (VM) for a single RhoGEF2 RNAi embryo ($n \geq 11$ cells/row; median 15 cells). (I) Box-and-whisker plot of minimum F-actin level relative to the highest-mean ectoderm row for each condition. *P*-values were based on Mann–Whitney U test (right) or Kruskal–Wallis+post hoc test (left). Scale bars: 10 μ m.

Wieschus, 2016), which could promote the ability of these cells to remodel, bend and stretch in response to mechanical stress (Stricker et al., 2010). In contrast, the neighboring ectoderm and the medial ventral cells have high lateral F-actin and AJ density, which may help those cells maintain their shape under stress (Rauzi et al., 2015). Although apical actin networks can modulate cell deformability (Dehapiot et al., 2020), the apical F-actin at this stage did not differ between mesoderm and ectoderm at the boundary. Therefore, differences in cell behavior could not be explained by different densities of apical F-actin.

F-actin regulation and function are typically tightly intertwined with both AJs and myosin. Our data suggest that cortical F-actin density is regulated independently of AJs, but *diaphanous* mutants and F-actin inhibiting drugs disrupt AJs (Homem and Peifer, 2008; Levayer et al., 2011; Mason et al., 2013). Whereas Diaphanous levels are comparable across the ectoderm-mesoderm boundary, the Cofilin activator Slingshot (Ssh) is required for differential F-actin levels between mesoderm and ectoderm, suggesting that this depletion is due to increased actin turnover (Jodoin et al., 2015). F-actin and myosin interact physically and often affect the organization of each other; for example, myosin is required to bundle and organize apical F-actin (Murrell et al., 2015). In the mesoderm, elevated lateral myosin, which has been previously observed (Gracia et al., 2019), coincided with elevated lateral F-actin in midline mesoderm cells. However, the observation that myosin and F-actin have distinct tissue patterns suggest that they may also play some unique roles in this process.

RhoA activity level determines the shape of actomyosin patterning

Nested within this zone of Snail-mediated F-actin depletion, Twist activity causes actomyosin accumulation via graded RhoA

activation. The combination of these overlapping transcriptional patterns allows for domains of different cell behaviors and mechanical properties within a tissue of uniform cell fate (the mesoderm). RhoGTPases are regulated by complex interactions between their activating GEFs and inhibiting GAPs in many contexts (Denk-Lobnig and Martin, 2019). In the ventral furrow specifically, interplay between C-GAP and RhoGEF2 tunes sub-cellular localization and dynamics of the contractile apparatus during folding (Mason et al., 2016). Here, we found that changes to C-GAP or RhoGEF2 levels, at a dose that did not strongly disrupt cell-level organization, changed the multicellular pattern of actomyosin levels across the ventral domain. C-GAP RNAi and RhoGEF2 O/E both widened the myosin gradient and elevated lateral F-actin density in the marginal mesoderm. These specific pattern changes can be explained by a model in which there is a graded activator (RhoGEF2) and a uniform inhibitor (C-GAP), which modulates the position and width of the gradient. The similarity between RhoGEF2 and myosin gradients could be due to a failure to detect low levels of more marginal RhoGEF2 or possible feedback in the RhoA pathway (Priya et al., 2015).

Our data show that the gradient shape is tuned by activator-inhibitor balance at the level of direct RhoA regulation, which is susceptible to hyperactivation. There are other points in the pathway where balance between inhibition and activation is important and could contribute to tissue-wide patterning. In particular, GPRK2, an inhibitor of GPCR signaling, affects myosin organization and cell behaviors (Fuse et al., 2013; Jha et al., 2018). In GPRK2 mutant embryos, apical constriction is expanded, such that marginal mesoderm cells that normally stretch accumulate myosin and constrict (Fuse et al., 2013).

Fold curvature is tuned by tissue-wide actomyosin patterning

Our disruptions of actomyosin patterns and the resulting changes in tissue shape suggest that the tissue-wide pattern of the actin cytoskeleton regulates shape. We showed experimentally and in simulations that changing myosin gradient width by modulating the levels of RhoGEF2 or C-GAP changes tissue curvature. Elevating RhoA activity moves the gradient outward, creating a region of uniformly high-myosin around the midline and resulting in low midline curvature. We determined that the width of the myosin gradient for an individual embryo during flattening is predictive of its furrow and post-fold shape. This is consistent with theoretical work that suggested a broader contractile domain would lower tissue curvature (Heer et al., 2017). We have extended this work by demonstrating how changes in RhoA activation level can ‘tune’ tissue curvature without altering mesoderm width. We disentangled the effects of myosin amplitude and gradient width *in silico*, showing that increasing width, but not amplitude, decreases curvature. Curvature in our simulations was lower than observed in experiments overall, suggesting that aspects other than myosin contractility, such as softening of lateral cells by F-actin depletion or non-elastic properties of cells, contribute to folding as well.

The fact that increased overall contractility in the tissue decreases fold curvature may seem counter-intuitive, but one has to consider the local and global force balance and competition between contractile cells in the tissue. For example, expanding the domain of contractile cells prevents efficient, anisotropic apical constriction at the ventral midline (Chanet et al., 2017; Heer et al., 2017), which we also observed for RhoGEF2 O/E embryos. RhoGEF2 overexpression resulted in elevated contractility specifically in the mesoderm, presumably because RhoGEF2 is autoinhibited and

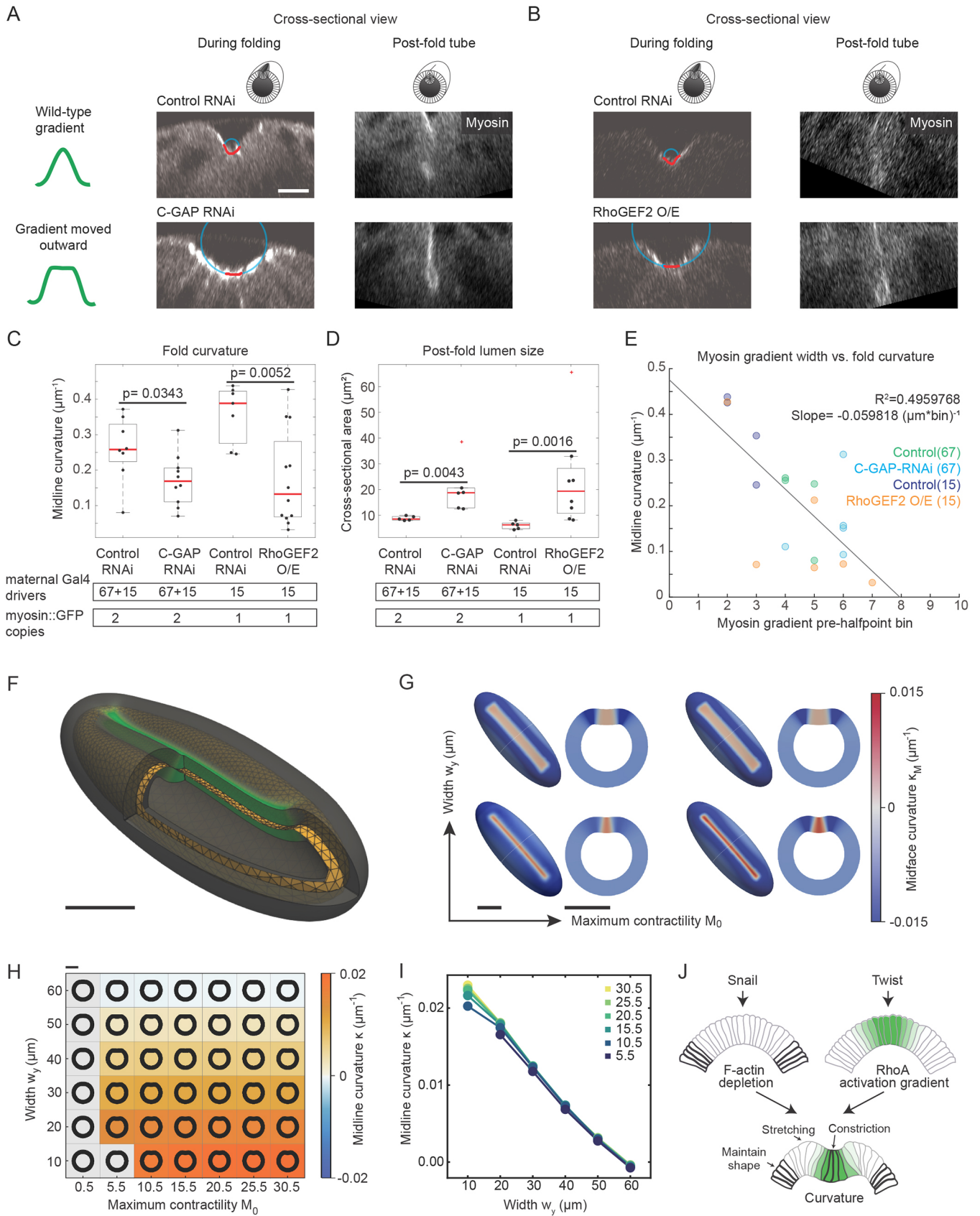


Fig. 7. See next page for legend.

Fig. 7. The contractile gradient width affects furrow curvature and lumen size. (A,B) Cross-sectional rescues during and after folding of control (Rh3 RNAi) and C-GAP RNAi (A) or control and RhoGEF2 O/E (B) embryos expressing sqh::GFP (myosin) and gap43::mCherry (membranes, not shown). Images were rotated to orient ventral side up and black pixels added at corners. (C,D) Quantification of midline curvature (circle fit to surface outline – red dots and cyan circle in A and B; three measurements averaged per embryo) (C) and lumen size (D) for C-GAP RNAi and RhoGEF2 O/E embryos with respective controls. Data are represented by box-and-whisker plots. *P*-values are based on pairwise comparison with Mann–Whitney U test. (E) Regression analysis of the relationship between myosin gradient width and curvature for control, C-GAP RNAi and RhoGEF2 O/E embryos. Gradient width was determined as the most dorsal bin with mean intensity higher than half-maximal. Curvature was measured as in C. $F=15.6$, $P\text{-value}=0.00103$ (*F*-statistic versus constant model). (F) 3D rendering of the numerical continuum mechanics model consisting of a triangulated midface surface (yellow), approximating the full embryo geometry. An experimentally derived spatial myosin distribution (green) modulates the midface curvature and induces furrow formation. An interactive Embryo Atlas of simulations with different myosin patterns can be found at https://bzjan.github.io/embryo_atlas/. (G) Midface curvature on 3D embryo shape and cross sections illustrates dependence of furrow shape on myosin-distribution width and amplitude. Simulation parameters are listed in the Supplementary Materials and Methods. (H) Dependence of midline curvature (circle fit to apical surface curvature at 10 μm invagination depth, corresponding to experimental measurements) on myosin-distribution width and amplitude with overlaid cross sections in black. (I) Midline apical surface curvatures decay with larger widths (and smaller amplitudes) of the myosin field. Different colored lines represent different myosin amplitudes (5.5–30.5). (J) Model for the regulation of tissue-wide patterning in the ventral furrow. See Discussion for explanation. Scale bar: 10 μm (A,B); 100 μm (F,G,H).

only becomes active in response to $G_{\alpha 12/13}$ signaling (Garcia De Las Bayonas et al., 2019). In many other cases, it has been shown that the successful constriction and invagination of cells depends on neighboring tissue mechanics (Ko et al., 2020; Perez-Mockus et al., 2017; Sui et al., 2018). A recent study has showed that marginal mesoderm cells can constrict if constriction is inhibited along the midline (Bhide et al., 2020 preprint).

Development generates a multitude of different curvatures and shapes for different contexts. We showed that tissue curvature is sensitive to changes in the pattern of actomyosin within the mesoderm, suggesting that gene expression patterning is an effective way to tune curvature. Given the importance of this patterning mechanism in regulating tissue shape, it is likely that mechanical cell properties are patterned and tuned across tissues similarly in other developmental contexts with different curvature requirements.

MATERIALS AND METHODS

Fly stocks and crosses

For maternal gene depletion and overexpression, crosses were made between maternal GAL4 drivers and UAS-driven constructs. Embryos laid by F1 females were imaged and analyzed. For RhoGEF2- and C-GAP RNAi, females carrying a UAS-driven short hairpin RNA were crossed to maternal GAL4 drivers containing fluorescent markers (See Table S1 for specific lines). F1 females were collected and mated to sibling males, reared at 25°C unless otherwise indicated and embryos from this cross were imaged. A similar strategy was used to overexpress RhoGEF2 using a UAS>RhoGEF2 line.

For Phalloidin-stained *snail* mutant embryos, a *halo snail*/CyO – sqh::GFP stock was used to identify zygotic *snail* mutants. Individual *halo* embryos were collected and fixed (as described below). We confirmed the presence of the *snail* mutant by staining with anti-Snail, which we found was disrupted in *halo* embryos. The two *snail* mutant embryos also labeled with Sqh::GFP were individually selected based on the *halo* phenotype and the other was identified from bulk embryo fixation based on the abnormal Snail localization. For live imaging of Utrophin::mCherry in *twist* or *snail* mutants, Utrophin::mCherry/CyO was crossed with *halo twist* (or *snail*)/CyO – sqh::GFP and non-curly

winged *halo twist* (or *snail*)/Utrophin::mCherry virgin females were collected and crossed to *twist* (or *snail*)/CyO – sqh::GFP males. Gastrulation in embryos from this final cross were live imaged to identify mutants (based on failure to invaginate mesoderm) and early time points in these movies were used to assess the lateral F-actin pattern.

A C-terminal GFP tag was inserted at the endogenous C-GAP locus using CRISPR-Cas9 as previously described (Gratz et al., 2015). Coding sequences for two 15 base pair (bp) gRNAs targeting neighboring sites 5' of the *rhoGAP71E* gene start codon were cloned into the pU6-BbsI plasmid using the CRISPR Optimal Target Finder (Gratz et al., 2014; Iseli et al., 2007). The donor template plasmid for homology directed repair was generated using Exponential Megaprimering PCR (Ulrich et al., 2012). A plasmid backbone (from pHD scarless DS Red) containing an ampicillin resistance gene and an origin of replication was combined with two homology arms (1219 bp and 1119 bp) homologous to the region around the *rhoGAP71E* gene start codon, flanking a GFP-encoding DNA sequence (kindly provided by Iain Cheeseman, Whitehead Institute, Massachusetts Institute of Technology, Cambridge, MA, USA) with an N-terminal four amino acid-encoding linker region (Ser-Gly-Gly-Ser). Both plasmids were injected into nanos>Cas9-expressing embryos. Surviving adults were crossed to *y, w; +;+flies* and then screened for mosaic GFP insertion using PCR. Progeny of GFP-positive injected flies were crossed to *y, w; +; Dr/TM3 flies* and then screened by PCR for the GFP insertion. Successful insertions were further analyzed by sequencing. The fly stock established from their offspring was later back-crossed once to OreR flies in order to eliminate potential off-target mutations.

Live and fixed imaging

Embryos were collected in plastic cups covered with apple-juice agar plates. Flies were allowed to lay eggs for 2–4 h at 25°C unless otherwise indicated (Table S1). The plate was removed and the embryos immersed in Halocarbon 27 oil for staging. Cellular blastoderm-stage embryos were collected and prepared for imaging. Embryos were dechorionated with 50% bleach, rinsed with water, and then mounted on a slide with embryo glue (Scotch tape resuspended in heptane), with the ventral side facing upwards. A chamber was made with two 1.5 coverslips as spacers, a 1.0 coverslip placed on top, and the chamber was filled with Halocarbon 27 oil before imaging. Images were acquired on a Zeiss 710 microscope with an Aplanachromat 40 \times /1.2 numerical aperture W Korr M27 objective at 25°C.

Immuno- and Phalloidin staining was performed using standard methods (Martin et al., 2009). Embryos were dechorionated in 50% bleach, fixed with 4% paraformaldehyde/heptane for 30 min, devitellinized manually, stained with Phalloidin, primary antibodies and appropriate fluorescently tagged secondary antibodies, and mounted in AquaPolymount (Polysciences). Anti-snail (rabbit, 1:100; M. Biggin, Lawrence Berkeley National Lab, CA, USA), anti-GFP (rabbit, 1:500; Abcam, ab290), anti-Diaphanous (rabbit, 1:5000; S. Wasserman, University of California, San Diego, CA, USA) and anti-E-cadherin [rat, 1:50; Developmental Studies Hybridoma Bank (DSHB)] antibodies and AlexaFluor568 Phalloidin (0.01 U/ μl , Invitrogen) were used. For anti- α -catenin (rat, 1:50; DHSB), anti-armadillo (mouse, 1:500; DHSB) and anti-snail antibody co-stainings, embryos were dechorionated, heat-fixed in boiling Triton salt solution (0.3% Triton-X, 0.7 M NaCl), placed on ice and devitellinized by vortexing in 1:1 heptane:methanol. After three washes with methanol, embryos were antibody stained as above. All imaging was carried out on a Zeiss 710 confocal microscope with a Plan-Apochromat 40 \times /1.2 numerical aperture W Korr M27 objective. For microscope settings used in imaging, refer to Table S2.

Gradient analysis

Cell-based analysis was carried out as described previously (Heer et al., 2017). All image analysis was performed in Fiji (<http://fiji.sc>) (Schindelin et al., 2012) and MATLAB (MathWorks). Custom software for image processing is available upon request.

Definition of developmental timing

Wild-type embryos were staged based on the time of folding. The accuracy of this method was confirmed by comparing constricted areas per bin at the

selected time point. For embryos with disrupted constriction and folding, an analogous time point was chosen relative to the beginning of myosin/fluorescence accumulation.

Shell projection and thresholding to measure apical fluorescence intensity

Shell projections of the apical surface were made to capture the embryo surface. First, cytoplasmic background signal [defined as the mean cytoplasmic signal+2.5 standard deviations (s.d.)] was subtracted from the myosin channel (Martin et al., 2009; Vasquez et al., 2014). For non-myosin fluorescent signal (Fig. 5), the cytoplasmic background subtraction was adjusted to account for differences in signal-to-noise ratio for different fluorescent markers (RhoGEF2-GFP: mean+2 s.d.; aniRBD-GFP: mean+2 s.d., rok-GFP: mean+2.5-3 s.d.).

The maximum myosin (or other apically enriched fluorescent) signal intensity in the z -plane was used to generate a rough map of the embryo surface. A Fourier transform was used to generate a smooth continuous surface. Myosin signal was averaged over the 4 μm above the surface of detected maximum intensity and membrane signal was the sum of the signal from 1 μm below the surface. A Gaussian blur filter (radius 1 pixel or 0.2125 μm for fluorescent signal, 0.7-1 pixels for membranes) was applied after shell projection to reduce noise.

Shell projections from live and immunostained images were then segmented using an existing MATLAB package, Embryo Development Geometry Explorer (EDGE) (Gelbart et al., 2012). Membrane signal (Gap43::mCherry) or cortical actin (Phalloidin) projections were used to detect cell boundaries (and track cells in time for live images). Errors in segmentation were corrected manually. Our segmentation algorithm was used to determine centroid position, cell diameter, cell area and cell perimeter of segmented cells as well as total apical myosin/fluorescence signal per cell based on the corresponding myosin/fluorescent channel projection.

Defining cell bins

For all image quantifications, data was aggregated into ‘cell bins’ (Heer et al., 2017). Cells were assigned to bins based on the ventral-dorsal position of the cell centroid relative to the ventral midline. The ventral midline was defined as the position at which the furrow closes. In fixed images or for embryos that did not fold (or rotated while folding), the position of the ventral midline was determined by symmetry of the fluorescent signal. Live images with several segmented time points were binned based on initial position of the cell centroid before constriction and folding; the boundaries of the bins were set based on the average cell diameter along the ventral-dorsal axis. For images in which cells had already started to constrict, the width of each bin was set manually (but still relative to average cell diameter) to approximate the width of cells at that ventral-dorsal position. We used Matlab to generate box-and-whisker plots depicting the distribution of data, overlaid with the mean of each bin. For box-and-whisker plots, bottom and top sides of the box represent 25th and 75th percentile of cells, respectively. Midline is the median and red points are outliers; defined as values 1.5 times bigger than the interquartile range. Fluorescence signal was normalized by dividing by the mean of the bin with highest average intensity, to adjust for variability in imaging conditions.

Fitting and quantifying cell-based gradient properties

To quantify differences in gradient shape, myosin levels by bin were fit to logistic function of the form $y=a/(1+e^{-b(x-c)})$. Upper and lower limits and initial guesses for each variable were, respectively, a : 0, ∞ , mean position at first bin; b : $-\infty$, ∞ , 1; c : 1, last bin of dataset, 6. The variable c is the inflection point of the fitted curve and was used as a measurement of gradient width for each embryo and plotted in a box-and-whisker plot overlaid with data points representing each embryo.

Myosin profiles based on physical distance

In addition to cell-based analysis of myosin gradients, we analyzed myosin profiles based on physical distances for higher throughput (Fig. 6C,D). For this analysis, shell projections were loaded in Fiji and a line plot across the ventral-dorsal axis, averaging all anterior to posterior positions, was

generated. Shell projections were fit to a function of the form $y=a \times 0.5 \times (1 + \tanh(s(x - (x_0 - 0.5 \times w)))) \times 0.5 \times (1 + \tanh(-s(x - (x_0 + 0.5 \times w))))$ in Matlab using the fit function. Upper and lower limits and initial guesses for each variable were, respectively: a : 0, ∞ , maximum y value; s : $-\infty$, ∞ , 30; w : 0, ∞ , 20; x_0 : $-\infty$, ∞ , 0.

For plotting physical distance traces, the ventral midline for each embryo was identified and then both sides of the plot were averaged for each embryo as for cell-based analysis. Mean and standard deviation of multiple embryos was shown.

The half-maximal width of fitted curves was used to statistically compare differences in gradient width. For paired groups, the non-parametric Mann–Whitney U test (Matlab ‘ranksum’) was used at a 0.05 significance level. For groups compared with the same control, the Kruskal–Wallis non-parametric test (Matlab ‘kruskalwallis’) with Tukey’s honest significant difference criterion for posthoc testing (Matlab ‘multcompare’) was used to determine which pairs were significantly different. Results were shown as box-and-whisker plots overlaid with data points representing each embryo and P -values and sample sizes reported in the figure legend. Some fits were used to determine ‘myosin’ patterning in simulation (see Theoretical simulations).

Lateral F-actin quantification

For apical projections of Phalloidin staining (that included the apical part of lateral F-actin signal) (Figs 1B,C and 3D), embryos were shell-projected and cells tracked similarly to myosin and other markers (see above), but no background subtraction was required because of the low background staining for Phalloidin-stained embryos. For analysis, lateral signal was extracted from the apical shell projection by only using signal within 2 μm of the tracked cell boundaries. This total lateral F-actin signal was divided by the cell perimeter to obtain lateral F-actin density independently of cell circumference.

Because mesodermal F-actin depletion was most obvious subapically, not apically, live images with Utrophin::GFP (Fig. 2B,D; Fig. 6E,G; Fig. S1D) were ‘shell-projected’ in Fiji by generating a z -reslice (1 μm per slice) and then doing a second reslice along a manually drawn, subapical segmented line that followed the ventral-dorsal curvature of the embryo surface at around 12–17 μm below the surface (Fig. S3A). This allowed us to account for specific ventral-dorsal curvature and get an image of the tissue at a consistent apical-basal depth. Images that required visualization of nuclear snail staining were also subapically projected (Fig. 2A; Fig. S2A; Fig. S6C). For analysis, the central region along the anterior-posterior (AP) axis of the shell-projection (~80–110 μm), where AP curvature is small, was used to quantify F-actin (Utrophin::mCherry or ::GFP) intensity along the ventral-dorsal axis. For analysis of the tissue-wide pattern, lateral signal was extracted from the subapical shell projection by only using signal within 2 μm of the tracked cell boundaries. This total lateral F-actin signal was divided by the cell perimeter to obtain lateral F-actin density independent of cell size. F-actin traces were normalized to the maximum mean signal in the ectoderm (bin 7 and above), except in *twist* mutants, in which the mesoderm was narrower (normalized to highest mean between bin 3 and above).

The maximal depletion (1–minimum lateral F-actin density) (within bins 3–10) normalized to the maximum in the ectoderm (bins 7 and above) was used to statistically compare differences in F-actin depletion between conditions (Fig. 6I). For paired groups, the non-parametric Mann–Whitney U test (Matlab ‘ranksum’) was used at a 0.05 significance level. For groups compared with the same control, the Kruskal–Wallis non-parametric test (Matlab ‘kruskalwallis’) with Tukey’s honest significant difference criterion for posthoc testing (Matlab ‘multcompare’) was used to determine which pairs were significantly different. Results were shown as box-and-whisker plots and P -values and sample sizes reported in the figure legend.

Pulsing analysis

Images of live embryos with myosin and membrane markers during folding were obtained as above, but with faster scan speed and smaller z -depth, to obtain time steps between 6 and 10 s, which is sufficient to capture typical myosin and area pulsing behavior (Martin et al., 2009). Cells across the mesoderm were tracked over time using EDGE; cell area and myosin intensity were exported. In Matlab 2019a, we detected peaks within individual cells of

maximal myosin intensity increase by smoothing with a moving average filter and then detecting local maxima. The myosin intensity and cell area behavior ~ 100 s before and after each maximum was saved as a trace. Pulse traces were averaged for each cell bin to identify average behavior based on ventral-dorsal cell position. Myosin persistence was defined as the minimum myosin intensity within each trace after a myosin pulse minus the minimum myosin intensity before the same pulse. Persistence of area constriction was defined as the maximum cell area after a myosin pulse minus maximum cell area before the same pulse. Persistence values were averaged by bin and plotted in Matlab for three individual embryos.

To analyze how the relationship between area and myosin behaviors changes based on cell position, we cross-correlated myosin and area behavior (as described in Martin et al., 2009). We used the 'xcorr' function in Matlab to cross-correlate the change in myosin intensity (myosin intensity at a time point minus myosin intensity at the previous time point) with constriction change (cell area at a time point minus cell area at the next time point, i.e. positive value if constricting, negative if stretching) for each cell trace. Cross-correlations for each cell were averaged by bin (distance from the midline) and plotted.

Curvature analysis

Movies with at least 20 μm z-depth were resliced in Fiji to create transverse virtual cross sections (1 μm thickness) of the ventral furrow all along the AP axis of the embryo. Apically enriched myosin signal was used to trace the apical surface of the folding tissue with the freehand line tool in Fiji. Traces were made for a cross section at the center of the AP axis of the embryo as well as for cross sections 20 μm anterior and posterior. The time point of measurement was chosen based on invagination depth (~ 10 μm). The xy coordinates of each trace were imported into Matlab R2019a. After manually determining the position of the ventral midline, a circle fit (Taubin method; <https://www.mathworks.com/matlabcentral/fileexchange/22678-circle-fit-taubin-method>) was applied to the central part of the trace, 2.5 μm left and right of the midline. The inverse of the fitted circle radius was defined as the fold curvature. The three traces taken from each embryo were averaged to obtain the fold curvature value for that embryo.

Post-folding lumina were visualized from central cross sections of the same embryos, the curvature of which had been analyzed and measured for a single AP position. Lumen area was determined by manually fitting an ellipse to the lumen in each cross-section in Fiji and measuring its area.

Curvature and lumen measurements were compared between genotypes using the non-parametric two-sample Mann-Whitney U test ('ranksum' command in Matlab).

Regression analysis

All linear regression fits (Fig. 1E; Fig. 7E) were performed in Matlab R2019a using the 'fitlm' command. The original data as well as the best fit line were plotted and the R-squared value was reported as a measure of fit. Significance was determined by *F*-test, which tests if the regression model fits significantly better than a model with just a constant term (flat line), and *P*- and *F*-values were reported.

For myosin gradients, the position of the most dorsal bin with myosin levels above half-maximal was used to describe gradient width. This bin position was then compared with central curvature measurements of the same embryo at a later time point (at ~ 10 μm invagination depth, analyzed with circle fit).

Quantitative RT-PCR

To verify knockdown efficiency for RNAi lines, we used q-RT-PCR to measure *rhoGAP71E* or *RhoGEF2* mRNA levels in control and C-GAP RNAi, or control and RhoGEF2 RNAi and RhoGEF2-O/E embryos, respectively.

RNA extraction

Fifteen cellular blastoderm and early gastrula embryos (see Table S1 for fly lines used) were collected for each sample and crushed in Trizol using an electric pestle. The mRNA was extracted using Trizol:Chloroform 5:1 extraction, the top aqueous phase was transferred and precipitated with 1:1 ethanol with 5% 0.1:1 3 M NaOAc (30-60 min at -20°C). Samples were

centrifuged (12,000 *g*) and washed with 70% ethanol at 4°C three times and with 100% ethanol once, centrifuging at 7500 *g* after each wash. The mRNA-containing pellets were resuspended in 15 μl water and then treated with DNase (Invitrogen Turbo DNA-free kit). RNA concentrations were measured by NanoDrop.

Reverse transcription

cDNA was generated from extracted mRNA with the Invitrogen SuperScriptTM III First-Strand Synthesis System. Briefly, 8 μl of mRNA sample (up to 5 μg) were incubated with oligo(dT)₂₀ primers and dNTPs at 65°C for 5 min, then cDNA was generated by adding buffer, 0.2 vol 25 mM MgCl₂, 0.1 vol 0.1 M DTT, 40 U RNaseOUT and 200 U SuperScript III Reverse Transcriptase to each reaction and elongating at 50°C for 50 min. Reactions were terminated at 85°C for 5 min and 2 U of RNase H added for 20 min at 37°C .

Quantitative PCR

Exon-exon junction-spanning primers for 70-100 bp regions of *RhoGEF2*, *rhoGAP71E* and *rpl18* (housekeeping gene) were designed based on suggestions from Harvard Medical School DRSC/TRIP Functional Genomics Resources: *RhoGEF2* forward: TGAAAACGCAAGCAAA-TCTG, reverse: GATGCCACACCTTCTTCGAT; *rhoGAP71E* forward: AAAACGAAGCCGAGCAAACG, reverse: GAATGTGCCGAACAGT-AGAAT; *rpl18* forward: ATCCCAGGATGTGTACCTGC, reverse: TGATGCGGTTGAACCTTCTGT.

Primer functionality was verified using conventional PCR

qPCR was conducted with the Applied BiosystemsTM StepOnePlusTM Real-Time PCR System and Applied BiosystemsTMPowerUpTM SYBRTM Green Master Mix. Four technical replicates were set up for each reaction, for all combinations of controls and *rhoGAP71E* and *RhoGEF2* disruptions with their respective primers, as well as *rpl18* housekeeping gene primers. In addition, no template controls without cDNA were set up for each primer pair. Reaction mixes consisted of 5 μl Master Mix, 0.5 μl of 10 mM forward and reverse primer, 6 ng cDNA template (volume calculated based on previous mRNA quantifications with NanoDrop) and nuclease-free water up to 10 μl . The qPCR cycling mode consisted of an initial 2 min UDG inactivation at 50°C , 2 min at 95°C , followed by 40 cycles of 95°C for 15 s (denaturing), 55°C for 15 s (annealing) and 72°C for 1 min. Melt curve analysis was conducted after all cycles were finished.

To analyze results using the $\Delta\Delta C_T$ method, C_T values for each reaction were downloaded from the thermocycler. Mean C_T values and standard error were determined from technical replicates for each condition. ΔC_T values were calculated by subtracting *rpl18* C_T from gene-of-interest C_T values and standard error was calculated by Gaussian error propagation. $\Delta\Delta C_T$ values were calculated by subtracting ΔC_T in matching control RNAi conditions from ΔC_T in C-GAP RNAi, RhoGEF2 O/E or RhoGEF2 RNAi conditions. Standard error was again calculated by Gaussian error propagation. Fold gene expression change was calculated as $2^{-\Delta\Delta C_T}$. Top and bottom of error bars was calculated as $2^{-(\Delta\Delta C_T + SE)}$ and $2^{-(\Delta\Delta C_T - SE)}$, respectively.

Theoretical simulations

Refer to Supplementary Materials and Methods. An interactive Embryo Atlas of simulations with different myosin patterns can be found at https://bzjan.github.io/embryo_atlas/.

Note added in proof

During the final preparation of this manuscript, a study was published providing evidence that anterior-posterior patterning synergizes with dorsal-ventral patterning for polarize lateral myosin (John and Rauzi, 2021).

Acknowledgements

We thank N. Perrimon, L. Perkins and the Transgenic RNAi Project at Harvard Medical School (National Institutes of Health/National Institutes of General Medical Sciences R01-GM084947) for providing transgenic RNAi stocks. We thank V. Tserunyan for the software adapted here to analyze myosin pulses. We thank B. Adhikary for help with analysis of F-actin levels and Jennifer Nwako for images of

wild-type embryos used in Fig. S2. We thank current and former Martin lab members for helpful discussions and feedback.

Competing interests

The authors declare no competing or financial interests.

Author contributions

Conceptualization: M.D.-L., J.F.T., N.C.H., J.D., A.C.M.; Methodology: M.D.-L., J.F.T., N.C.H.; Software: M.D.-L., J.F.T., N.C.H.; Validation: M.D.-L.; Formal analysis: M.D.-L., J.F.T.; Investigation: M.D.-L., J.F.T., N.C.H.; Data curation: M.D.-L., N.C.H.; Writing - original draft: M.D.-L., A.C.M.; Writing - review & editing: M.D.-L., J.F.T., J.D., A.C.M.; Visualization: M.D.-L., J.F.T.; Supervision: J.D., A.C.M.; Project administration: A.C.M.; Funding acquisition: A.C.M., J.D.

Funding

This work was supported by a grant from the National Institutes of General Medical Sciences (R01GM125646 to A.C.M.), by the Alexander von Humboldt-Stiftung Feodor Lynen Fellowship to J.F.T. and the Massachusetts Institute of Technology Robert E. Collins Distinguished Scholarship Fund to J.D. This work was supported in part by a National Institutes of Health Pre-Doctoral Training Grant (T32GM007287). Deposited in PMC for release after 12 months.

Peer review history

The peer review history is available online at <https://journals.biologists.com/dev/article-lookup/doi/10.1242/dev.199232>

References

- Baillies, A., Collinet, C., Philippe, J.-M., Lenne, P.-F., Munro, E. and Lecuit, T. (2019). Genetic induction and mechanochemical propagation of a morphogenetic wave. *Nature* **572**, 467-473. doi:10.1038/s41586-019-1492-9
- Barrett, K., Leptin, M. and Settlemann, J. (1997). The Rho GTPase and a putative RhoGEF mediate a signaling pathway for the cell shape changes in *Drosophila* gastrulation. *Cell* **91**, 905-915. doi:10.1016/S0092-8674(00)80482-1
- Bhida, S., Gombalova, D., Mönke, G., Stegmaier, J., Zinchenko, V., Kreshuk, A., Belmonte, J. M. and Leptin, M. (2020). Mechanical competition alters the cellular interpretation of an endogenous genetic programme. *BioRxiv*.
- Boulay, J. L., Dennefeld, C. and Alberga, A. (1987). The *Drosophila* developmental gene snail encodes a protein with nucleic acid binding fingers. *Nature* **330**, 395-398. doi:10.1038/330395a0
- Bun, P., Dmitrieff, S., Belmonte, J. M., Nédélec, F. J. and Lénárt, P. (2018). A disassembly-driven mechanism explains F-actin-mediated chromosome transport in starfish oocytes. *eLife* **7**, e31469. doi:10.7554/eLife.31469
- Chanet, S. and Schweisguth, F. (2012). Regulation of epithelial polarity by the E3 ubiquitin ligase Neuralized and the Bearded inhibitors in *Drosophila*. *Nat. Cell Biol.* **14**, 467-476. doi:10.1038/ncb2481
- Chanet, S., Miller, C. J., Vaishnav, E. D., Ermentrout, B., Davidson, L. A. and Martin, A. C. (2017). Actomyosin meshwork mechanosensing enables tissue shape to orient cell force. *Nat. Commun.* **8**, 15014. doi:10.1038/ncomms15014
- Clément, R., Dehapiot, B., Collinet, C., Lecuit, T. and Lenne, P.-F. (2017). Viscoelastic dissipation stabilizes cell shape changes during tissue morphogenesis. *Curr. Biol.* **27**, 3132-3142.e4. doi:10.1016/j.cub.2017.09.005
- Coravos, J. S. and Martin, A. C. (2016). Apical sarcomere-like Actomyosin contracts nonmuscle *Drosophila* epithelial cells. *Dev. Cell* **39**, 346-358. doi:10.1016/j.devcel.2016.09.023
- Costa, M., Wilson, E. T. and Wieschaus, E. (1994). A putative cell signal encoded by the folded gastrulation gene coordinates cell shape changes during *Drosophila* gastrulation. *Cell* **76**, 1075-1089. doi:10.1016/0092-8674(94)90384-0
- Dawes-Hoang, R. E., Parmar, K. M., Christiansen, A. E., Phelps, C. B., Brand, A. H. and Wieschaus, E. F. (2005). folded gastrulation, cell shape change and the control of myosin localization. *Development* **132**, 4165-4178. doi:10.1242/dev.01938
- Dehapiot, B., Clément, R., Alégot, H., Gászó-Gerhát, G., Philippe, J.-M. and Lecuit, T. (2020). Assembly of a persistent apical actin network by the formin Frl/Fmnl tunes epithelial cell deformability. *Nat. Cell Biol.* **22**, 791-802. doi:10.1038/s41556-020-0524-x
- Denk-Lobnig, M. and Martin, A. C. (2019). Modular regulation of Rho family GTPases in development. *Small GTPases* **10**, 122-129. doi:10.1080/21541248.2017.1294234
- Dubuis, J. O., Tkacik, G., Wieschaus, E. F., Gregor, T. and Bialek, W. (2013). Positional information, in bits. *Proc. Natl. Acad. Sci. USA* **110**, 16301-16308. doi:10.1073/pnas.1315642110
- Fernandez-Gonzalez, R. and Zallen, J. A. (2011). Oscillatory behaviors and hierarchical assembly of contractile structures in intercalating cells. *Phys. Biol.* **8**, 045005. doi:10.1088/1478-3975/8/4/045005
- Fernandez-Gonzalez, R., Simoes Sde, M., Röper, J.-C., Eaton, S. and Zallen, J. A. (2009). Myosin II dynamics are regulated by tension in intercalating cells. *Dev. Cell* **17**, 736-743. doi:10.1016/j.devcel.2009.09.003
- Foe, V. E. (1989). Mitotic domains reveal early commitment of cells in *Drosophila* embryos. *Development* **107**, 1-22. doi:10.1242/dev.107.1.1
- Fox, D. T. and Peifer, M. (2007). Abelson kinase (Abl) and RhoGEF2 regulate actin organization during cell constriction in *Drosophila*. *Development* **134**, 567-578. doi:10.1242/dev.02748
- Furlong, E. E. M., Andersen, E. C., Null, B., White, K. P. and Scott, M. P. (2001). Patterns of gene expression during *Drosophila* mesoderm development. *Science* **293**, 1629-1633. doi:10.1126/science.1062660
- Fuse, N., Yu, F. and Hirose, S. (2013). Gprk2 adjusts Fog signaling to organize cell movements in *Drosophila* gastrulation. *Development* **140**, 4246-4255. doi:10.1242/dev.093625
- García De Las Bayonas, A., Philippe, J.-M., Lellouch, A. C. and Lecuit, T. (2019). Distinct RhoGEFs activate apical and junctional contractility under control of G proteins during epithelial morphogenesis. *Curr. Biol.* **29**, 3370-3385.e7. doi:10.1016/j.cub.2019.08.017
- Gelbart, M. A., He, B., Martin, A. C., Thiberge, S. Y., Wieschaus, E. F. and Kaschube, M. (2012). Volume conservation principle involved in cell lengthening and nucleus movement during tissue morphogenesis. *Proc. Natl. Acad. Sci. USA* **109**, 19298-19303. doi:10.1073/pnas.1205258109
- Gracia, M., Theis, S., Proag, A., Gay, G., Benassayag, C. and Suzanne, M. (2019). Mechanical impact of epithelial-mesenchymal transition on epithelial morphogenesis in *Drosophila*. *Nat. Commun.* **10**, 2951. doi:10.1038/s41467-019-10720-0
- Gratz, S. J., Ukken, F. P., Rubinstein, C. D., Thiede, G., Donohue, L. K., Cummings, A. M. and O'Connor-Giles, K. M. (2014). Highly specific and efficient CRISPR/Cas9-catalyzed homology-directed repair in *Drosophila*. *Genetics* **196**, 961-971. doi:10.1534/genetics.113.160713
- Gratz, S. J., Harrison, M. M., Wildonger, J. and O'Connor-Giles, K. M. (2015). Precise genome editing of *Drosophila* with CRISPR RNA-Guided Cas9. *Methods Mol. Biol.* **1311**, 335-348. doi:10.1007/978-1-4939-2687-9_22
- Großhans, J. and Wieschaus, E. (2000). A genetic link between morphogenesis and cell division during formation of the ventral furrow in *Drosophila*. *Cell* **101**, 523-531. doi:10.1016/S0092-8674(00)80862-4
- Hacker, U. and Perrimon, N. (1998). DRhoGEF2 encodes a member of the Dbl family of oncogenes and controls cell shape changes during gastrulation in *Drosophila*. *Genes Dev.* **12**, 274-284. doi:10.1101/gad.12.2.274
- Heer, N. C., Miller, P. W., Chanet, S., Stoop, N., Dunkel, J. and Martin, A. C. (2017). Actomyosin-based tissue folding requires a multicellular myosin gradient. *Development* **144**, 1876-1886. doi:10.1242/dev.146761
- Homem, C. C. F. and Peifer, M. (2008). Diaphanous regulates myosin and adherens junctions to control cell contractility and protrusive behavior during morphogenesis. *Development* **135**, 1005-1018. doi:10.1242/dev.016337
- Hong, L., Dumond, M., Tsugawa, S., Sapala, A., Routier-Kierzkowska, A.-L., Zhou, Y., Chen, C., Kiss, A., Zhu, M., Hamant, O. et al. (2016). Variable cell growth yields reproducible Organ Development through spatiotemporal averaging. *Dev. Cell* **38**, 15-32. doi:10.1016/j.devcel.2016.06.016
- Iseli, C., Ambrosini, G., Bucher, P. and Jongeneel, C. V. (2007). Indexing strategies for rapid searches of short words in genome sequences. *PLoS ONE* **2**, e579. doi:10.1371/journal.pone.0000579
- Jha, A., van Zanten, T. S., Philippe, J.-M., Mayor, S. and Lecuit, T. (2018). Quantitative control of GPCR organization and signaling by endocytosis in epithelial morphogenesis. *Curr. Biol.* **28**, 1570-1584.e6. doi:10.1016/j.cub.2018.03.068
- Jodoin, J. N., Coravos, J. S., Chanet, S., Vasquez, C. G., Tworoger, M., Kingston, E. R., Perkins, L. A., Perrimon, N. and Martin, A. C. (2015). Stable force balance between epithelial cells arises from F-Actin turnover. *Dev. Cell* **35**, 685-697. doi:10.1016/j.devcel.2015.11.018
- John, A. and Rauzi, M. (2021). A two-tier junctional mechanism drives simultaneous tissue folding and extension. *Dev. Cell* **56**, 1469-1483.e5. doi:10.1016/j.devcel.2021.04.003
- Kerridge, S., Munjal, A., Philippe, J.-M., Jha, A., de las Bayonas, A. G., Saurin, A. J. and Lecuit, T. (2016). Modular activation of Rho1 by GPCR signalling imparts polarized myosin II activation during morphogenesis. *Nat. Cell Biol.* **18**, 261-270. doi:10.1038/ncb3302
- Ko, C. S., Kalakuntla, P. and Martin, A. C. (2020). Apical constriction reversal upon mitotic entry underlies different morphogenetic outcomes of cell division. *Mol. Biol. Cell* **31**, 1663-1674. doi:10.1091/mbc.E19-12-0673
- Kolsch, V., Seher, T., Fernandez-Ballester, G. J., Serrano, L. and Leptin, M. (2007). Control of *Drosophila* gastrulation by apical localization of adherens junctions and RhoGEF2. *Science* **315**, 384-386. doi:10.1126/science.1134833
- Leptin, M. (1991). twist and snail as positive and negative regulators during *Drosophila* mesoderm development. *Genes Dev.* **5**, 1568-1576. doi:10.1101/gad.5.9.1568
- Leptin, M. (2005). Gastrulation movements: the logic and the nuts and bolts. *Dev. Cell* **8**, 305-320. doi:10.1016/j.devcel.2005.02.007
- Leptin, M. and Grunewald, B. (1990). Cell shape changes during gastrulation in *Drosophila*. *Development* **110**, 73-84. doi:10.1242/dev.110.1.73
- Levayer, R. and Lecuit, T. (2013). Oscillation and polarity of E-cadherin asymmetries control actomyosin flow patterns during morphogenesis. *Dev. Cell* **26**, 162-175. doi:10.1016/j.devcel.2013.06.020

- Levayer, R., Pelissier-Monier, A. and Lecuit, T. (2011). Spatial regulation of Dia and Myosin-II by RhoGEF2 controls initiation of E-cadherin endocytosis during epithelial morphogenesis. *Nat. Cell Biol.* **13**, 529-540. doi:10.1038/ncb2224
- Lim, B., Levine, M. and Yamazaki, Y. (2017). Transcriptional pre-patterning of *Drosophila* Gastrulation. *Curr. Biol.* **27**, 610. doi:10.1016/j.cub.2017.01.067
- Manning, A. J., Peters, K. A., Peifer, M. and Rogers, S. L. (2013). Regulation of epithelial morphogenesis by the G protein-coupled receptor mist and its ligand fog. *Sci. Signal.* **6**, ra98. doi:10.1126/scisignal.2004427
- Martin, A. C., Kaschube, M. and Wieschaus, E. F. (2009). Pulsed contractions of an actin-myosin network drive apical constriction. *Nature* **457**, 495-499. doi:10.1038/nature07522
- Martin, A. C., Gelbart, M., Fernandez-Gonzalez, R., Kaschube, M. and Wieschaus, E. F. (2010). Integration of contractile forces during tissue invagination. *J. Cell Biol.* **188**, 735-749. doi:10.1083/jcb.200910099
- Mason, F. M., Tworoger, M. and Martin, A. C. (2013). Apical domain polarization localizes actin-myosin activity to drive ratchet-like apical constriction. *Nat. Cell Biol.* **15**, 926-936. doi:10.1038/ncb2796
- Mason, F. M., Xie, S., Vasquez, C. G., Tworoger, M. and Martin, A. C. (2016). RhoA GTPase inhibition organizes contraction during epithelial morphogenesis. *J. Cell Biol.* **214**, 603-617. doi:10.1083/jcb.201603077
- Mitrossilis, D., Röper, J.-C., Le Roy, D., Driquez, B., Michel, A., Ménager, C., Shaw, G., Le Denmat, S., Ranno, L., Dumas-Bouchiat, F. et al. (2017). Mechano-transductive cascade of Myo-II-dependent mesoderm and endoderm invaginations in embryo gastrulation. *Nat. Commun.* **8**, 13883. doi:10.1038/ncomms13883
- Mongera, A., Rowghanian, P., Gustafson, H. J., Shelton, E., Kealhofer, D. A., Carn, E. K., Serwane, F., Lucio, A. A., Giammona, J. and Campàs, O. (2018). A fluid-to-solid jamming transition underlies vertebrate body axis elongation. *Nature* **561**, 401-405. doi:10.1038/s41586-018-0479-2
- Munjal, A., Philippe, J.-M., Munro, E. and Lecuit, T. (2015). A self-organized biomechanical network drives shape changes during tissue morphogenesis. *Nature* **524**, 351-355. doi:10.1038/nature14603
- Murrell, M., Oakes, P. W., Lenz, M. and Gardel, M. L. (2015). Forcing cells into shape: the mechanics of actomyosin contractility. *Nat. Rev. Mol. Cell Biol.* **16**, 486-498. doi:10.1038/nrm4012
- Nikolaïdou, K. K. and Barrett, K. (2004). A Rho GTPase signaling pathway is used reiteratively in epithelial folding and potentially selects the outcome of Rho activation. *Curr. Biol.* **14**, 1822-1826. doi:10.1016/j.cub.2004.09.080
- Oda, H. and Tsukita, S. (2001). Real-time imaging of cell-cell adherens junctions reveals that *Drosophila* mesoderm invagination begins with two phases of apical constriction of cells. *J. Cell Sci.* **114**, 493-501. doi:10.1242/jcs.114.3.493
- Perez-Mockus, G., Mazouni, K., Roca, V., Corradi, G., Conte, V. and Schweisguth, F. (2017). Spatial regulation of contractility by Neuralized and Bearded during furrow invagination in *Drosophila*. *Nat. Commun.* **8**, 1594. doi:10.1038/s41467-017-01482-8
- Priya, R., Gomez, G. A., Budnar, S., Verma, S., Cox, H. L., Hamilton, N. A. and Yap, A. S. (2015). Feedback regulation through myosin II confers robustness on RhoA signalling at E-cadherin junctions. *Nat. Cell Biol.* **17**, 1282-1293. doi:10.1038/ncb3239
- Rahimi, N., Averbukh, I., Carmon, S., Schejter, E. D., Barkai, N. and Shilo, B.-Z. (2019). Dynamics of Spaetzle morphogen shuttling in the *Drosophila* embryo shapes gastrulation patterning. *Development* **146**, dev181487. doi:10.1242/dev.181487
- Rauzi, M., Krzic, U., Saunders, T. E., Krajnc, M., Zihler, P., Hufnagel, L. and Leptin, M. (2015). Embryo-scale tissue mechanics during *Drosophila* gastrulation movements. *Nat. Commun.* **6**, 8677. doi:10.1038/ncomms9677
- Rembold, M., Ciglar, L., Yanez-Cuna, J. O., Zinzen, R. P., Girardot, C., Jain, A., Welte, M. A., Stark, A., Leptin, M. and Furlong, E. E. M. (2014). A conserved role for Snail as a potentiator of active transcription. *Genes Dev.* **28**, 167-181. doi:10.1101/gad.230953.113
- Rogers, K. W. and Schier, A. F. (2011). Morphogen gradients: from generation to interpretation. *Annu. Rev. Cell Dev. Biol.* **27**, 377-407. doi:10.1146/annurev-cellbio-092910-154148
- Roth, S., Stein, D. and Nüsslein-Volhard, C. (1989). A gradient of nuclear localization of the dorsal protein determines dorsoventral pattern in the *Drosophila* embryo. *Cell* **59**, 1189-1202. doi:10.1016/0092-8674(89)90774-5
- Rushlow, C. A., Han, K., Manley, J. L. and Levine, M. (1989). The graded distribution of the dorsal morphogen is initiated by selective nuclear transport in *Drosophila*. *Cell* **59**, 1165-1177. doi:10.1016/0092-8674(89)90772-1
- Salbreux, G., Charras, G. and Paluch, E. (2012). Actin cortex mechanics and cellular morphogenesis. *Trends Cell Biol.* **22**, 536-545. doi:10.1016/j.tcb.2012.07.001
- Schindelin, J., Arganda-Carreras, I., Frise, E., Kaynig, V., Longair, M., Pietzsch, T., Preibisch, S., Rueden, C., Saalfeld, S., Schmid, B. et al. (2012). Fiji: an open-source platform for biological-image analysis. *Nat. Methods* **9**, 676-682. doi:10.1038/nmeth.2019
- Simoes Sde, M., Blankenship, J. T., Weitz, O., Farrell, D. L., Tamada, M., Fernandez-Gonzalez, R. and Zallen, J. A. (2010). Rho-kinase directs Bazooka/Par-3 planar polarity during *Drosophila* axis elongation. *Dev. Cell* **19**, 377-388. doi:10.1016/j.devcel.2010.08.011
- Spahn, P. and Reuter, R. (2013). A vertex model of *Drosophila* ventral furrow formation. *PLoS ONE* **8**, e75051. doi:10.1371/journal.pone.0075051
- Steward, R. (1989). Relocalization of the dorsal protein from the cytoplasm to the nucleus correlates with its function. *Cell* **59**, 1179-1188. doi:10.1016/0092-8674(89)90773-3
- Steward, R., Zusman, S. B., Huang, L. H. and Schedl, P. (1988). The dorsal protein is distributed in a gradient in early *Drosophila* embryos. *Cell* **55**, 487-495. doi:10.1016/0092-8674(88)90035-9
- Stricker, J., Falzone, T. and Gardel, M. L. (2010). Mechanics of the F-actin cytoskeleton. *J. Biomech.* **43**, 9-14. doi:10.1016/j.jbiomech.2009.09.003
- Sui, L., Alt, S., Weigert, M., Dye, N., Eaton, S., Jug, F., Myers, E. W., Jülicher, F., Salbreux, G. and Dahmann, C. (2018). Differential lateral and basal tension drive folding of *Drosophila* wing discs through two distinct mechanisms. *Nat. Commun.* **9**, 4620. doi:10.1038/s41467-018-06497-3
- Sumigra, K. D., Terwilliger, M. and Lechler, T. (2018). Morphogenesis and compartmentalization of the intestinal Crypt. *Dev. Cell* **45**, 183-197.e5. doi:10.1016/j.devcel.2018.03.024
- Sweeton, D., Parks, S., Costa, M. and Wieschaus, E. (1991). Gastrulation in *Drosophila*: the formation of the ventral furrow and posterior midgut invaginations. *Development* **112**, 775-789. doi:10.1242/dev.112.3.775
- Thisse, B., Stoezel, C., Gorostiza-Thisse, C. and Perrin-Schmitt, F. (1988). Sequence of the twist gene and nuclear localization of its protein in endomesodermal cells of early *Drosophila* embryos. *EMBO J.* **7**, 2175-2183. doi:10.1002/j.1460-2075.1988.tb03056.x
- Ulrich, A., Andersen, K. R. and Schwartz, T. U. (2012). Exponential megapriming PCR (EMP) cloning—seamless DNA insertion into any target plasmid without sequence constraints. *PLoS ONE* **7**, e53360. doi:10.1371/journal.pone.0053360
- Vasquez, C. G., Tworoger, M. and Martin, A. C. (2014). Dynamic myosin phosphorylation regulates contractile pulses and tissue integrity during epithelial morphogenesis. *J. Cell Biol.* **206**, 435-450. doi:10.1083/jcb.201402004
- von Dassow, M. and Davidson, L. A. (2009). Natural variation in embryo mechanics: gastrulation in *Xenopus laevis* is highly robust to variation in tissue stiffness. *Dev. Dyn.* **238**, 2-18. doi:10.1002/dvdy.21809
- Weng, M. and Wieschaus, E. (2016). Myosin-dependent remodeling of adherens junctions protects junctions from Snail-dependent disassembly. *J. Cell Biol.* **212**, 219-229. doi:10.1083/jcb.201508056
- Wolpert, L. (1969). Positional information and the spatial pattern of cellular differentiation. *J. Theor. Biol.* **25**, 1-47. doi:10.1016/S0022-5193(69)80016-0
- Xie, S. and Martin, A. C. (2015). Intracellular signalling and intercellular coupling coordinate heterogeneous contractile events to facilitate tissue folding. *Nat. Commun.* **6**, 7161. doi:10.1038/ncomms8161
- Yevick, H. G., Miller, P. W., Dunkel, J. and Martin, A. C. (2019). Structural redundancy in Supracellular Actomyosin networks enables robust tissue folding. *Dev. Cell* **50**, 586-598.e3. doi:10.1016/j.devcel.2019.06.015